From depth-averaging to fully three-dimensional modelling of debris-flow dynamics

Journal of Power Sources 614 (2024) 235043

Contents lists available at ScienceDirect

Journal of Power Sources

journal homepage: www.elsevier.com/locate/jpowsour

Sustainable conversion of vine shoots and pig manure into high-performance anode materials for sodium-ion batteries

Darío Alvira [a,b,*], Daniel Antorán [a,b], Hamideh Darjazi [c], Giuseppe Antonio Elia [c], Victor Sebastian [b,d,e,f], Joan J. Manyà [a,b,**]

[a] Aragón Institute for Engineering Research (I3A), Thermochemical Processes Group, University of Zaragoza, Escuela Politécnica Superior, Crta. de Cuarte S/n, 22071, Huesca, Spain
[b] Department of Chemical Engineering and Environmental Technologies, University of Zaragoza, Campus Río Ebro, María de Luna 3, 50018, Zaragoza, Spain
[c] Group for Applied Materials and Electrochemistry—GAME Lab, Department of Applied Science and Technology—DISAT, Politecnico di Torino, 10129, Torino, Italy
[d] Instituto de Nanociencia y Materiales de Aragón (INMA), CSIC-Universidad de Zaragoza, Zaragoza, Spain
[e] Networking Research Center on Bioengineering Biomaterials and Nanomedicine (CIBER-BBN), Madrid, Spain
[f] Laboratorio de Microscopías Avanzadas, Universidad de Zaragoza, 50018, Zaragoza, Spain

HIGHLIGHTS

- Hydrothermal pretreatment boosts the performance of vine shoots-based anodes.
- Pig manure was successfully valorized as hydrothermal medium.
- Pig manure improves the capacity and stability of the resulting HC-based anodes.
- HCl addition promotes mesoporosity and the formation of microsphere clusters.
- The performance of HCs further improves when using diglyme-based electrolytes.

GRAPHICAL ABSTRACT

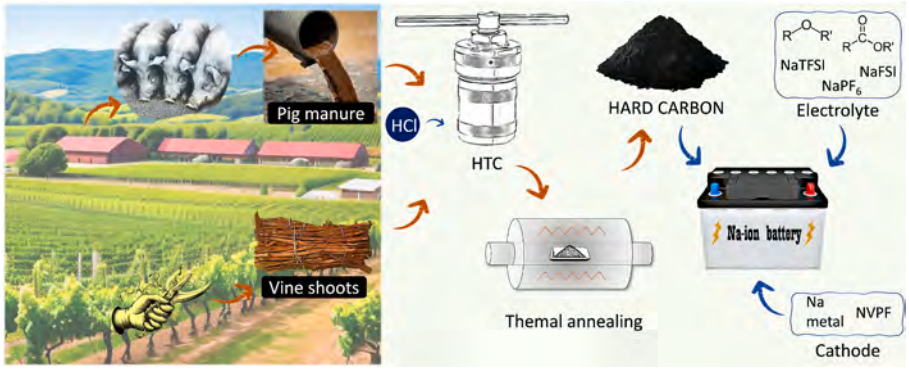

ARTICLE INFO

Keywords:
Sodium-ion battery
Hydrothermal carbonization
Hard carbon
Heteroatom doping
Pig manure
Diglyme

ABSTRACT

Sodium-ion batteries (SIBs) are considered promising candidates for future grid energy storage, with hard carbons emerging as key commercial anode materials. This study presents a novel approach to synthesize N-doped hard carbons via co-hydrothermal treatment of vine shoots and pig manure and subsequent thermal annealing of the resulting hydrochar. This method enhances the development of micro- and ultra-microporosity in the synthesized hard carbons, with nitrogen, and to a lesser extent phosphorus and sulfur, introduced as doping elements. Furthermore, the incorporation of hydrochloric acid during the hydrothermal step promotes biomass hydrolysis, leading to increased mesoporosity and the formation of microsphere clusters. In the realm of

* Corresponding author. Aragón Institute for Engineering Research (I3A), Thermochemical Processes Group, University of Zaragoza, Escuela Politécnica Superior, Crta. de Cuarte S/n, 22071, Huesca, Spain.
** Corresponding author. Aragón Institute for Engineering Research (I3A), Thermochemical Processes Group, University of Zaragoza, Escuela Politécnica Superior, Crta. de Cuarte S/n, 22071, Huesca, Spain.
E-mail addresses: dalvira@unizar.es (D. Alvira), joanjoma@unizar.es (J.J. Manyà).

https://doi.org/10.1016/j.jpowsour.2024.235043
Received 4 April 2024; Received in revised form 16 June 2024; Accepted 8 July 2024
Available online 14 July 2024

electrochemical performance, an investigation into various ester- and ether-based electrolytes has revealed $NaPF_6$ in diglyme as the best formulation, thanks to its thinner and more stable solid electrolyte interface (SEI). Using this electrolyte, the best-performing electrode showed an initial Coulombic efficiency (ICE) of 73 %, with reversible capacities of 239, 180, 86, and 57 mAh g^{-1} at 0.1, 1, 5, and 10 A g^{-1}, respectively. In addition, the electrode exhibited a remarkable capacity retention of 88 % after 250 cycles as well as a compatible behavior when paired with a NVPF-based cathode.

1. Introduction

Sodium-ion batteries (SIBs) are positioned as one of the most promising contenders to lead the next generation of large-scale electrochemical energy storage systems, which are essential for supporting the integration of intermittent renewable sources into the grid [1]. Nevertheless, the successful implementation of this technology depends on great part on the development of high-performance anode materials, as the storage capacity of sodium ions in graphite (using traditional ester-based electrolytes) is very limited, due to the thermodynamically unstable nature of sodium-graphite intercalation compounds [2]. Among various intercalation materials, hard carbons (HCs) stand out as the most promising candidates given their ability to store Na ions in their surface functionalities, defects, and pseudographitic domains [3]. Furthermore, there is a growing emphasis on HCs derived from biomass waste resources due to superior reversible capacities and environmental and cost-effectiveness considerations [4].

Herein, HCs were synthesized through thermochemical processing of vine shoots, a biowaste from wine-growing regions with an annual production ranging from 1.4 to 2.0 tons per hectare [5]. To transform this biowaste into a high-value material, we explored a hydrothermal treatment followed by a subsequent high-temperature annealing process. Biomass-derived hard carbons can preserve the inherent microstructure of the plant, resulting in a three-dimensional framework comprising pores and channels that facilitate electrolyte penetration, serving as pathways for Na ions and reservoirs for ion buffering [6]. Furthermore, carbon materials from biomass precursors usually possess a large number of defects and some remaining heteroatoms, together with randomly oriented pseudographitic domains [7]. The carbonization temperature plays a critical role in determining the final open and closed porosity, degree of graphitization, and surface chemistry. Therefore, for a given biomass feedstock, there exists an optimal temperature range, typically ranging from 1000 °C to 1400 °C, at which the maximum reversible capacity is achieved [8].

Hydrothermal carbonization (HTC) emulates the natural coal formation process and encompasses several reactions mechanisms, including hydrolysis, dehydration, decarboxylation, aromatization, and condensation polymerization [9]. Although hydrochar (i.e., the carbon material generated by HTC) does not meet the required characteristics to be used as electrode material, a cascaded HTC-pyrolysis synthesis approach could lead to engineered carbon-based electrodes. Compared with the direct pyrolysis strategy, HTC fosters pore enlargement and the creation of nanosphere domains enhancing the electrode reversible capacity [10–12]. Furthermore, HTC treatment enables the introduction of additional chemicals into the aqueous solution to facilitate specific decomposition or doping reactions. In this context, we investigated the catalytic role of HCl, as it is known to promote hydrolysis, deoxygenation, and the formation of spherical nanostructures [13].

On the other hand, the use of pig manure as a solvent in HTC is also assessed in the present study. During the period 2016–2019, more than 1400 million tons per year of farmyard manure were generated in the EU and UK [14]. Of this, more than 90 % was directly applied to soils as organic fertilizers. Concerning swine farming, the growing demand for meat drove a notable 25 % increase in pig numbers from 2010 to 2018, especially within highly intensive systems [15]. This entails an environmental challenge since pig production is considered a major contributor to global environmental concerns like carbon footprint, freshwater eutrophication, and ecosystem acidification [16]. In addition, its direct soil application can cause nutrient leaching and the release of toxic elements such as pathogens, antibiotics, and heavy metals [17]. Several recent studies also corroborate the prevalence in pig manure of bacteria with antibiotic resistance genes, posing a risk to both food safety and human health [18–20]. Therefore, exploring alternative treatments and uses for the proper management and valorization of this livestock waste is advisable.

Anaerobic digestion of manure [21], also mixed with biomass [22,23] has been studied to obtain biogas as well as a solid biofertilizer and water [24]. However, this process does not reduce the nitrogen content in the manure, thus failing to address the nitrate contamination issue. Furthermore, the utilization of ammonia removal systems (e.g., gas permeable membranes) is required to avoid the inhibition of methane production [25]. Composting [26,27] is another pathway that can be used to produce an organic fertilizer through organic matter degradation, pathogen destruction, and microbial stabilization. Nevertheless, solid-liquid separation is required to reach the optimal moisture content (60%–70 %) from the usual one (90%–98 %) contained in farmyard pig manures, what attached to long composting times, required abatement steps, and the release of sulfur volatiles and greenhouse gases [28,29], make this technology unattractive to be implemented at large scale.

Hydrothermal carbonization of pig manure—dried and mixed with other biomass feedstocks—has also been studied to produce hydrochar as solid fuel [30–33]. In addition, HTC offers a sustainable solution for converting these waste streams into more stable and valuable products such as biocarbons and biofertilizers, preventing the natural decomposition or fermentation of biomass and related CO_2 and CH_4 emissions. Recently, Ferrentino et al. [34] conducted a HTC study for the agronomical valorization of pig slurry, yielding a rich-carbon liquid fraction with appropriate contents of micronutrients, phosphorus, and nitrogen for fertigation; thereby mitigating the risk of eutrophication. Furthermore, in accordance with other authors [35–37], a significant portion of phosphorus and heavy metals coming from the manure are sequestered within the resulting hydrochar.

Regarding the carbon footprint, a life cycle assessment (LCA) performed by Owsianiak et al. [38] found that the carbon sequestration related to the hydrochar production should at least outweigh the global warming potential (GWP) derived of the manufacturing process and transportation to agricultural soils, while the environmental benefits notably increased when the hydrochar replaces less efficient biowaste management options like composting. Another LCA conducted by Ciceri et al. [39] estimated that producing one ton of hydrochar avoids CO_2 equivalent emissions in the range of 6.5–8.3 tons by taking into account activities related to coal mining, waste landfilling, and fossil fuel substitution. When pig manure was the raw biomass, the environmental benefits in terms of carbon sequestration can also be imperative. Davison et al. [40] calculated that the production of pig manure-derived hydrochar at 200 °C in the European Union could annually mitigate 17.16 million tons of $CO_{2\text{-eq}}$, increasing to 20.89 million tons with co-processing with grass.

The increasing interest in HTC technology for treating biomass materials has prompted numerous studies utilizing pilot plants to test and refine industrial processes in recent years [41–45]. Simultaneously, companies such as CarboREM SRL [46], OxyPower HTC™ [47], HTCycle AG [48], and TerraNova Energy GmbH [49] have developed industrial-scale continuous operating plants for hydrochar production.

Notably, Ingelia SL, after constructing its first industrial HTC plant (TRL 9) in 2010, which was capable of processing 6000 tons of biomass per year, now designs and installs modular HTC reactors—operating at 20 bars and 210 °C—under demand [50,51]. In 2021, the International Energy Agency (IEA) evaluated the feasibility of Ingelia's technology, projecting a plant capable of treating 78,000 tons/year of biowaste (70 % moisture content) and producing 15,400 tons/year of hydrochar. With a market price for hydrochar at 180 €/ton, the project estimated an internal rate of return (IRR) of 18.7 %, capital expenditure (CAPEX) of 351 €/ton of waste, and operational expenditure (OPEX) of 20 €/ton of waste, which aligns with market drivers [39]. This indicates that HTC for biomass wastes is a relatively mature technology that could be widely implemented in the short to medium term.

With all the above in mind, the present study aims to investigate, for the first time, the electrochemical behavior of vine shoot-derived hydrochars, produced using pig manure as the hydrothermal medium, as negative electrodes for SIBs. It is anticipated that pig manure, in addition to serve as solvent in the hydrothermal treatment, can effectively introduce N, P, and S heteroatoms into the structure of the resulting HC, thus enhancing its electrochemical behavior. Producing high-performance carbonaceous anodes from biomass-derived hydrochars would make the HTC process economically more attractive, supporting the valorization of agronomic residues into environmentally and agronomically beneficial products.

2. Experimental section

2.1. Materials

Vine shoots (*Vitis vinifera* L.), herein referred as VS, of the Cabernet Sauvignon variety were collected in the wine region of Somontano (Huesca province, Spain) and used as carbon precursor. The raw biomass was crushed to obtain a particle size below 0.7 mm. As documented in a previous study [52], proximate and elemental analyses, X-ray fluorescence (XRF) spectroscopy, and determination of key biomass constituents (hemicelluloses, cellulose, and lignin) were conducted. The pig manure was supplied by a finishing farm also located in the province of Huesca and the water content and chemical composition were determined using vacuum drying, elemental analysis, and XRF, respectively.

2.2. Production of hard carbons

Vine shoots-derived hard carbons were produced via a two-step carbonization approach as shown in Fig. S1 (Supplementary Information). First, 15 g of vine shoots were hydrothermally treated (in 50 g of DI water) for 12 h at 180 °C in a 100 mL volume PTFE-lined stainless-steel autoclave (Huanyu ZHT-172C) under autogenous pressure. The material was then collected through vacuum filtration and dried at 100 °C for 12 h. The obtained hydrochar was then placed in an alumina boat and carbonized at a heating rate of 5 °C min^{-1} up to 800, 1000 or 1200 °C (soaking time at the highest temperature of 2 h). For this purpose, a tubular mullite-made reactor inserted into a furnace (Carbolite TF1 16/60/300) under an Ar atmosphere was employed. The obtained HC was then grounded to powder (particle size below 90 μm), washed with a HCl solution (2 mol dm^{-3}) for 2 h at room temperature, and subsequently rinsed with DI water until neutral pH was achieved. The final product was denoted as HTC-*x*, where *x* refers to the highest carbonization temperature.

When pig manure was used as HTC solvent, the same procedure was followed using 50 g of manure instead of 50 g of water. In this case, the final product was denoted as HTC_{man}-*x*. Finally, additional HCs (HTC-1000ac and HTC_{man}-1000ac) were hydrothermally pretreated using a HCl 0.5 mol dm^{-3} solution of water and pig manure, respectively.

2.3. Characterization of produced hard carbons

Morphological assessment of HCs was conducted using an Inspect-F50A scanning electron microscope combined with energy dispersive X-ray spectroscopy (SEM-EDX) from FEI (The Netherlands). Further examination of carbon structure was carried out through high-resolution transmission electron microscopy (HR-TEM) using an image-corrected Titan microscope (FEI, The Netherlands), operating at 300 kV and equipped with a SuperTwin® objective lens and a CETCOR Cs-objective corrector from CEOS Company, enabling a point-to-point resolution of 0.08 nm. Interplanar distances were measured from HR-TEM images using Digitalmicrograph® software. X-ray photoelectron spectroscopy (XPS; AXIS Supra instrument from Kratos Analytical Ltd, UK) was employed to investigate heteroatom-containing functional groups on surface.

Structural characterization involved X-ray powder diffraction (XRD; Empyrean instrument from Malvern Panalytical, UK, $\lambda = 0.154$ nm) and Raman spectroscopy (Alpha 300 model from WITec, Germany, $\lambda = 532$ nm). The XRD spectra were used to calculate the interlayer space between graphene layers (d_{002}), the apparent crystallite thickness along the c-axis (L_c), the apparent crystallite width along the a-axis (L_a), and the number of graphene stacking layers (n) using the Bragg's law and Scherrer's equation. Raman spectra were analyzed by deconvolution into one Gaussian-shaped band (D3) and four Lorentzian-shaped bands (G, D1, D2, and D4), according to the methodology suggested by Sadezky et al. [53].

The meso- and microporosity of HCs were estimated based on N_2 adsorption isotherms at −196 °C (using an Autosorb-iQ-XR2 analyzer from Quantachrome, Anton Paar, Germany) after outgassing the samples at 150 °C for 8 h under vacuum. Specific surface area was calculated using the Brunauer-Emmett-Teller (BET) model, and pore size distribution was determined through a Non-Local Density Functional Theory (NLDFT) model implemented in the QuadraWin 6.0 software. The ultramicroporosity of HCs was estimated from CO_2 adsorption isotherms at 0 °C using the same instrument and a NLDFT model.

2.4. Electrochemical characterization

The electrochemical performance of active materials was assessed utilizing a three-electrode Swagelok T-cell prototype (for more details review our previous paper [54]). The working electrode was composed of 80 wt% hard carbon, 10 wt% acetylene black (conductive agent), and 5 wt% styrene-butadiene rubber (SBR) and 5 wt% sodium carboxymethyl cellulose (Na-CMC) as binders. A homogeneous slurry was obtained by mixing with DI water under vortex agitation. Then the electrode was coated on aluminum current collector (16 μm thickness) with a controlled thickness of 100 μm and a final mass loading of 2.36 ± 0.09 mg cm^{-2}. Finally, 12 mm diameter electrodes were obtained after punching and vacuum drying at 120 °C overnight.

The Swagelok cells were assembled in an Ar-filled glovebox from Mbraun (Germany) with O_2 and H_2O contents less than 0.5 ppm. Two sodium metal discs of 12 mm and 5 mm diameter were used as counter and reference electrodes, respectively, and two 190 μm thickness glass fiber filters (Prat Dumas, France) were employed as separator. The electrolyte (200 μL) was composed of a NaTFSI solution (1 mol dm^{-3}) in a mixture (1:1 vol) of dimethyl carbonate (DMC) and ethylene carbonate (EC). Additional electrolyte formulation was also employed for comparison purposes: 1 mol dm^{-3} solutions of NaFSI and $NaPF_6$ in both diglyme (DGM) and EC:DMC. Full cells were assembled in the same setup using a $Na_3V_2(PO_4)2F_3$ (NVPF) cathode provided by group of Prof. Ruffo [55], employing an anode/cathode specific capacity ratio of 0.04.

Electrochemical measurements were carried out using a SP-200 (Bio-Logic, France) and a BT-2000 (Arbin, USA) potentiostats within a temperature range of 19–22 °C and following a 5-h rest period. Galvanostatic charge/discharge (GCD) cycling was conducted within a potential window of 0.01–2.5 V (vs. Na^+/Na), whereas the cyclic voltammetry

Table 1
Results from ultimate and ash composition analysis of dried pig manure.

Ultimate analysis (wt. % in daf basis)	
C	29.93 ± 0.80
H	3.56 ± 0.17
N	2.43 ± 0.01
S	0.34 ± 0.03
Inorganic matter as equivalent oxides (wt. % of ash)	
K_2O	55.59 ± 0.48
Cl	18.76 ± 0.20
Na_2O	9.88 ± 0.33
CaO	8.20 ± 0.14
P_2O_5	2.46 ± 0.08
S	2.00 ± 0.07
SiO_2	0.98 ± 0.05
MgO	0.80 ± 0.01
Fe_2O_3	0.53 ± 0.03
CuO	0.30 ± 0.02
ZnO	0.13 ± 0.003
Al_2O_3	0.12 ± 0.014
MnO	0.08 ± 0.004
Other metals	0.35 ± 0.022

profiles were collected at a scan rate of 0.1 mV s^{-1} from 0.01 to 2 V. Galvanostatic intermittent titration (GITT) measurements were performed at a current density of 30 mA g^{-1}, a pulse time of 20 min, and relaxation periods at open circuit of 1 h. To assess the interfacial behavior of the electrodes, electrochemical impedance spectroscopy (EIS) measurements were performed during the first and tenth cycles (at E = 0.5 V). Measurements were taken with an AC amplitude of 10 mV across a frequency range from 200 kHz to 10 mHz.

3. Results and discussion

3.1. Features of the biomass source

The vineshoots employed in this study originate from the same batch employed in our preceding study [56]. This biomass, possessing a lignin content of 20.3 wt%, has proven to be a suitable precursor for the pyrolytic production of HC anodes for SIBs. The relatively elevated lignin content facilitates a certain degree of ordering while averting excessive graphitization. Furthermore, the low ash content of this biomass (1.08 wt%) renders it an appealing material for electrochemical applications. Regarding pig manure, the dry matter content post vacuum oven drying stands at 3.5 %. The chemical composition of the solid fraction is presented in Table 1, with nitrogen and sulfur contents determined as 2.43 and 0.34 wt%, respectively. Concerning inorganic matter, the elements detected via XRF fall within the expected range for other swine manures produced in Spanish pig farms [17]. Note the elevated content of inorganic species derived from the pigs' diet (e.g., K, Na, Ca, and P), along

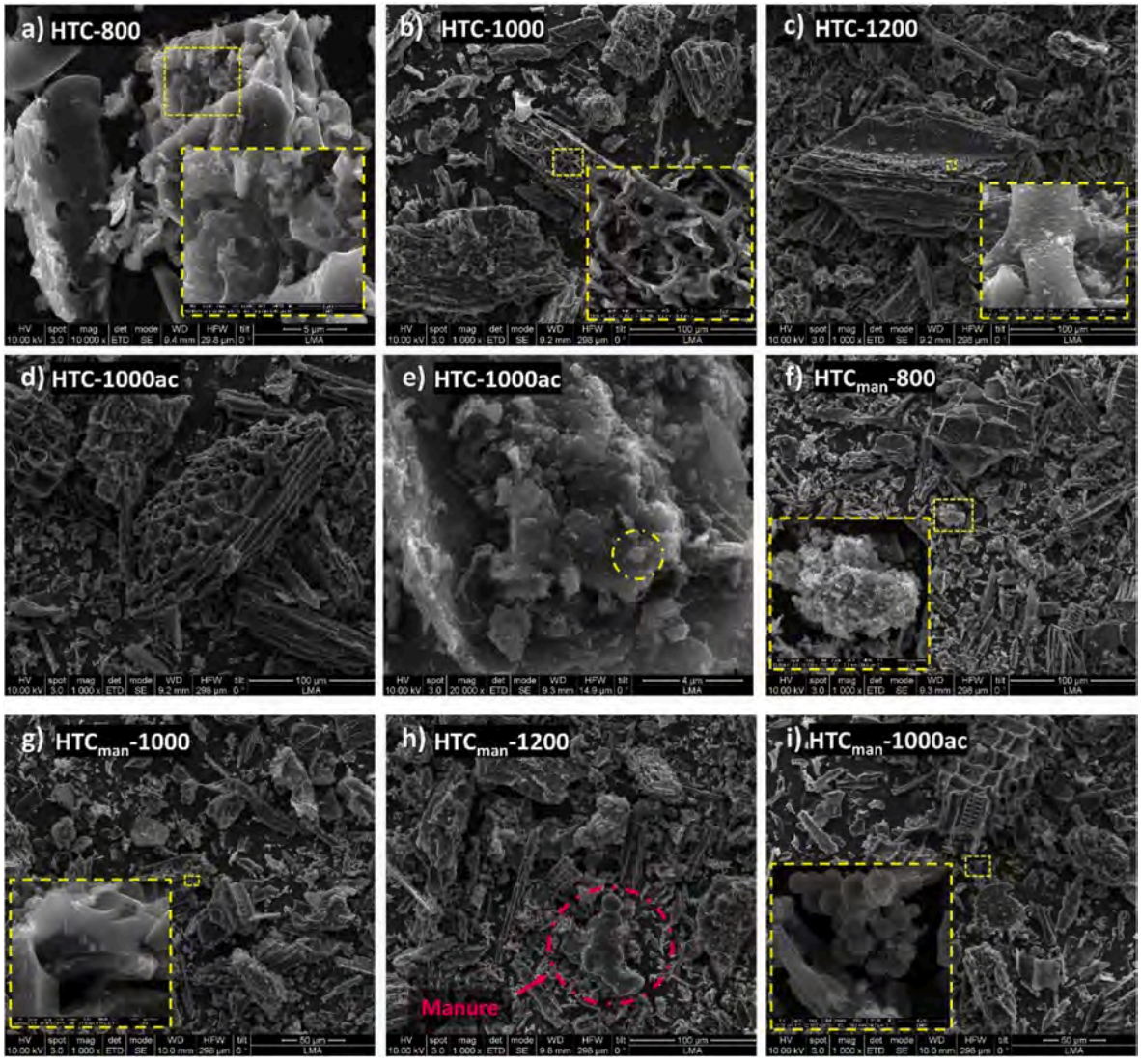

Fig. 1. SEM images of HTC-800 (a), HTC-1000 (b), HTC-1200 (c), HTC-1000ac (d) and (e), HTC_{man}-800 (f), HTC_{man}-1000 (g), HTC_{man}-1200 (h), and HTC_{man}-1000ac (i).

with the presence of certain heavy metals such as Cu and Zn, typically included in the feed as growth promoters.

3.2. Physicochemical characterization of HCs

Throughout the hydrothermal carbonization of biomass numerous reactions occur, yet the process is primarily governed by the hydrolysis reaction owing to its comparatively lower activation energy. Consequently, and in increasing order of temperature, ester and ether bonds within hemicellulose, cellulose, and lignin break down into smaller fragments. Subsequent dehydration and decarboxylation reactions also take place, responsible for reducing the H/C and O/C ratios [57]. Fig. 1 presents representative SEM images of all the HCs synthesized in this study. After HTC in water at 180 °C and successive carbonization at 800–1200 °C (see Fig. 1a–c) the biomass intrinsic support and transport structures remained. The preservation of these channels, macropores, and honeycomb-like structures becomes crucial since significantly contribute to the electrochemical performance of HCs. This is made possible by the high lignin content in the surrounding tissues, this polymer being the least susceptible to hydrolysis, with required temperatures above 250 °C [58]. On the other hand, as can be seen in the enlargements of SEM images, the most soluble carbohydrate components were transformed into new soft-shaped/spherical surface forms attached to the main structure's surface. When HCl was added in the hydrothermal step, discernible alterations in the morphology of pristine biomass were evident. For instance, cavity expansion and deformation of lignin-rich honeycomb complex walls, due to partial hydrolysis, can be observed in Fig. 1d, particularly in the upper-left corner. The acidic (HCl) hydrothermal medium also led to further fragmentation and the formation of discrete microspheres (see Fig. 1e).

The use of pig manure as hydrothermal medium resulted in the formation of new aggregates attached to the surface of the VS-derived carbon (see Fig. 1f), including some isolated microspheres. This can be explained by the relatively high proportion of soluble and easily accessible molecules for hydrolysis (such as proteins, carbohydrates, and fats) available in pig manure. In addition to these aggregates and microspheres adhered to the surface, the hydrothermal carbonization of pig manure can also lead to the formation of self-supported structures with lengths of up to 100 μm, as observed in Fig. 1h. Owing to the elevated soluble carbohydrate content, these molecules engender

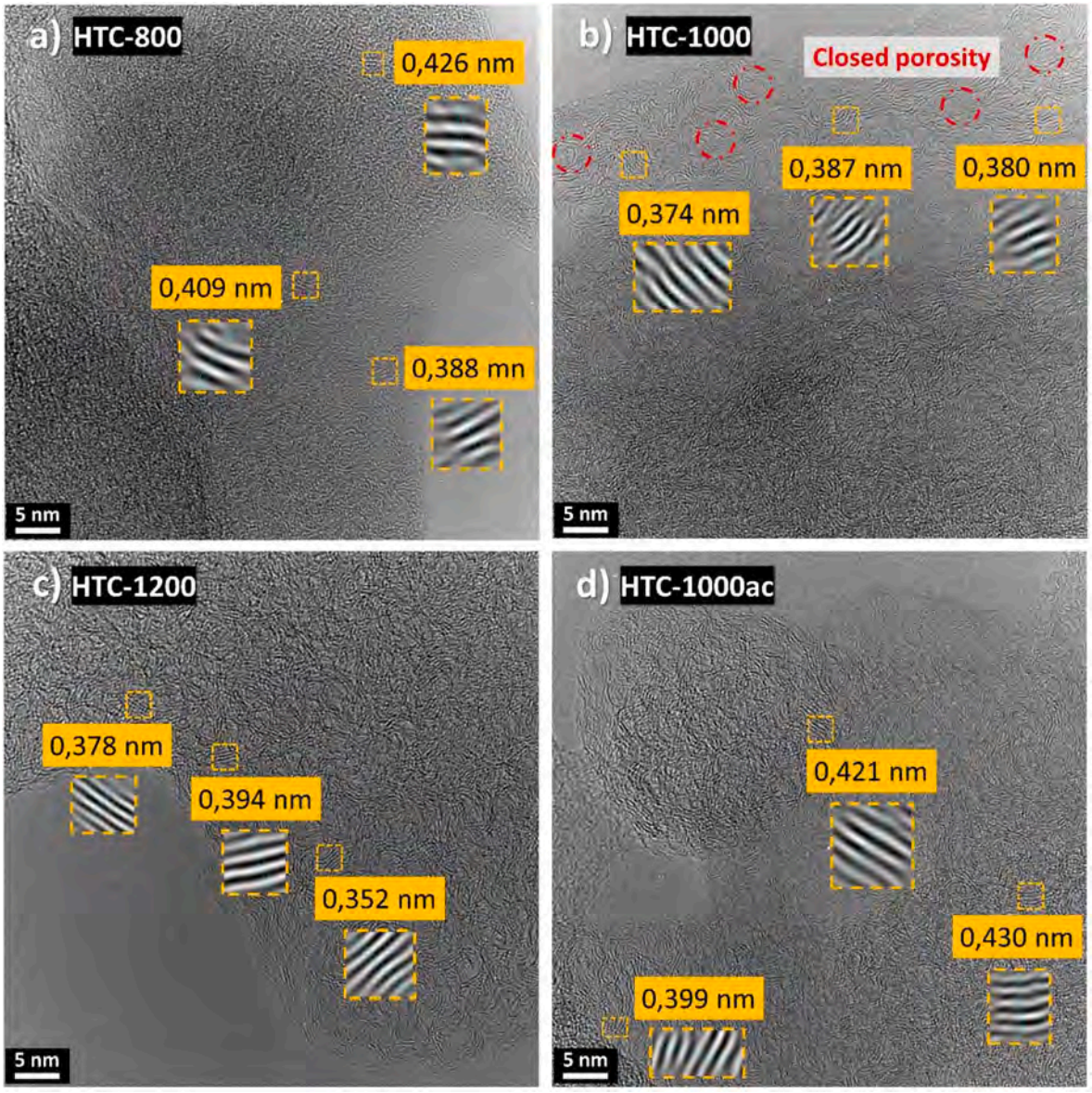

Fig. 2. HR-TEM images of HTC-800 (a), HTC-1000 (b), HTC-1200 (c), and HTC-1000ac (d).

complexes characterized by spherical morphologies and smooth contours, more akin to those derived from sugars and lipids [59,60]. When hydrochloric acid was used, the formation of microsphere clusters was enhanced (see Fig. 1i). The accumulation of microspheres results in a higher number of voids and conduits, which can create numerous paths for electrolyte permeation and establish a buffering zone for Na ions during desodiation.

HR-TEM images furnished insightful details regarding the degree of ordering at the subnanometric scale, morphologies, and growth of pseudographitic domains, as shown in Fig. 2 for HCs produced via HTC in water (Fig. 2a–c) and diluted hydrochloric acid media (Fig. 2d). With the elevation of the carbonization temperature, an increased degree of ordering was observed, coupled with a substantial development of closed porosity (see, for instance, Fig. 2b for the HTC-1000 sample). For the HTC-1000ac material (Fig. 2d), the presence of spherical forms promoted by the acidic medium were clearly visible, along with the voids generated between them. It is noteworthy that, for all HCs, the interlayer distances tend to exceed 0.37 nm, making them suitable for accommodating Na ions through the intercalation-deintercalation mechanism. Using HCl during the hydrothermal treatment appears to expand further these interlayer spaces, reaching d_{002} values greater than 0.4 nm, allowing the pseudoadsorption of Na ions according to the extended adsorption-insertion model [61]. HR-TEM images at lower magnification are also available in Fig. S2, showing a partial chemical

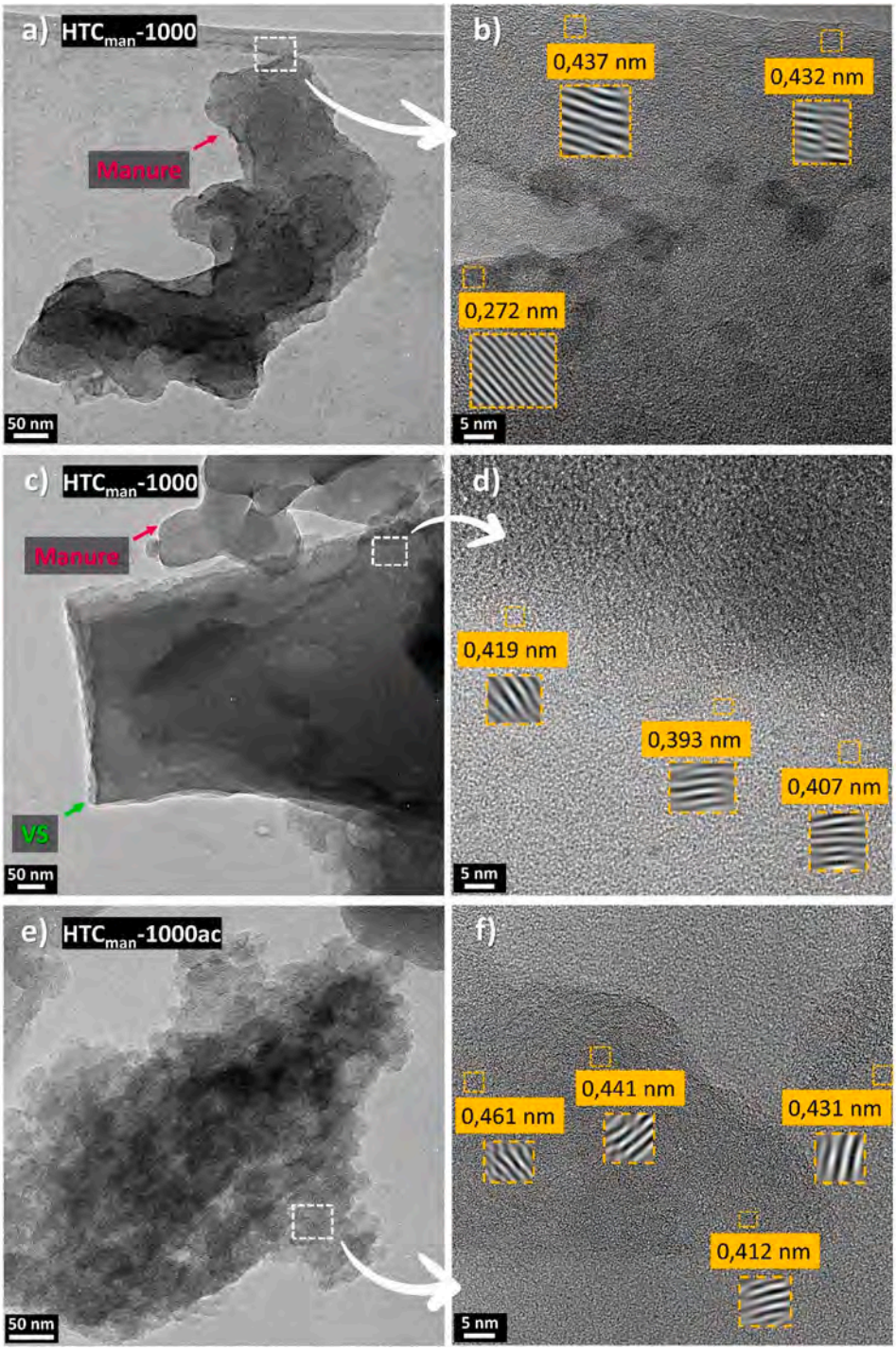

Fig. 3. HR-TEM images of HTC$_{man}$-800 (a), HTC$_{man}$-1000 (b), HTC$_{man}$-1200 (c), and HTC$_{man}$-1000ac (d).

reconstitution of the biomass into a sponge-like morphology, particularly under acidic hydrothermal conditions.

The HCs produced through HTC using pig manure as medium were also characterized via HR-TEM. Fig. 3a and b depict a carbon particle derived from the organic constituents of pig manure in the HTC_{man}-1000 sample. Within the matrix of a relatively amorphous carbonaceous structure, the conspicuous presence of well-ordered domains (with d_{002} values lower than 0.3 nm) is noteworthy. The existence of these well-ordered regions could be attributed not only to the nature of soluble organic substances in the manure, but also to the catalytic role of existing metals. On the other hand, when the magnification was taken from a vine shoot-derived particle (see Fig. 3c and d), the observed morphology closely resembled that found in HTC-1000, featuring a semi-ordered structure composed of groups of stacked graphitic layers. Lastly, when the hydrothermal process was conducted under acidic conditions (HTC_{man}-1000ac), it resulted in rounded carbon structures exhibiting the aforementioned sponge-like morphology (Fig. 3e and f). Enlarging this image reveals the presence of numerous pseudographitic domains with interlayer distances exceeding 0.440 nm, confirming the role of HCl in further expanding the interlayer spacing.

Concerning the XRD outcomes, Fig. S3 displays the patterns obtained for hard carbons. Two peaks are distinctly evident around 23° and 43°, aligning with the (002) crystal plane of graphitic sheets and the (100) plane of sp^2-hybridized hexagonal carbons, respectively. Table 2 reports the parameters calculated using the Bragg's law and Scherrer's equation, indicating consistency with the observations derived from both SEM and HR-TEM images. Regardless of the solvent used, an increase in the carbonization temperature led to higher degrees of graphitization (i.e., increased lengths of the pseudograpitic domains), more stacked graphitic layers, and a slight reduction in the d_{002} average interlayer distance. In addition, it is worth noting how the hydrothermal pretreatment of vine shoots appears to contribute to an increase in L_a values, in comparison with those reported in our previous study [56] for VS-derived HCs produced via slow pyrolysis and subsequent carbonization. Table 2 also lists the structural parameters calculated from the deconvoluted Raman spectra (available in Figs. S4 and S5). The values of both A_{D1}/A_G and L_a were consistent with the XRD findings explained above.

The CO_2 and N_2 adsorption isotherms for produced HCs are shown in Fig. S6. In line with the findings reported by Nieto et al. [62], the BET specific surface areas reported in Table 3 clearly indicate that the hydrothermal pretreatment of vine shoots promoted the development of both micro- and ultra-microporosity in the resulting HC, in comparison with the direct carbonization approach. For instance, HTC-800 yielded a CO_2 BET surface area of 445 $m^2\ g^{-1}$, significantly surpassing the 154 $m^2\ g^{-1}$ obtained in the above-mentioned previous study for a HC produced via carbonization at 800 °C without HTC pretreatment [56]. Table 3 also delineates the volumes of ultramicro-, micro-, and mesopores. In general terms, the use of pig manure did not seem to exert a great influence on the final porosity. However, its effect was dependent on the highest carbonization temperature. An increase from 800 to 1000 °C appears to yield minor changes, except for a slight decrease in microporosity and a minor increase in mesoporosity, which can likely be attributed to the collapse of some structures resulting in larger cavities. When the highest temperature rose further to 1200 °C, almost all ultramicropores disappeared, as thermal annealing induced the organization of graphene layers, leading to the contraction of narrow micropores, and even promoting melting and sintering processes [46]. When hydrochloric acid was used during the hydrothermal pretreatment (for both water and manure solvents), a marginal increase in the formation of ultramicropores was observed for a given carbonization temperature; however, HCl clearly promoted the development of a mesopore-rich structure, hitherto nonexistent, as observed in the pore size distribution plots available in Fig. S7.

With regards to the surface elemental composition, Fig. S8 displays SEM-EDX mapping measurements of HTC_{man}-x materials, highlighting, in pink, the aggregates derived from pig manure and, in green, the particles originating from vine shoots. For HCs carbonized at 800 and 1000 °C (Figs. S8a and S8b), it can be observed that the aggregates from pig manure exhibited a high N content (13%–15 %) and minor amounts of P and S. It is noteworthy that even at the highest temperature (1200 °C, Fig. S8c), in addition to the distinctive laminar and rugged morphology, the N content in this pig manure-derived complex remained around 10 %. This suggests that pig manure can be used as a green pathway for the heteroatom doping of lignocellulosic carbons. Nonetheless, with the addition of HCl (Fig. S8d), the availability of N and other heteroatoms on surface diminished dramatically. In agreement with Xie et al. [63], the catalytic role of HCl during the hydrolysis of organic matter could result in an enhanced transport of nitrogen and phosphorus from the solid to the liquid phase.

X-ray photoelectron spectroscopy (XPS) was employed across C 1s, N 1s, O 1s, S 2p, P 2p, and Ca 2p regions to unravel the surface chemistry of hard carbons (see Figs. S9–S16 for relevant spectra). Elemental contents derived from the survey XPS spectra revealed a high carbon content exceeding 93 at.% in all samples, alongside an increase in the quantities of nitrogen, phosphorus, and sulfur in carbons synthesized in the presence of pig manure (see Table S1). Deconvolution of C 1s high-resolution spectra (see Table 4) indicated that an increase in the highest carbonization temperature resulted in a larger proportion of sp^2-bonded C atoms at the expense of sp^3-bonded ones, as well as a decline in C—O bonds. This behavior is consistent with the gradual reduction in the number of defects as the carbonization temperature was higher. In contrast, when HCs were pretreated via HCl-catalyzed HTC, a slight increase in the proportion of sp^3 carbons was observed. This is consistent with the lower degree of graphitization deduced for these HCs from both XRD and Raman data. Concerning N- and S-containing functionalities (see Table 5), higher carbonization temperatures imply a progressive disappearance of oxygenated SO_x and N—O bonds, as well as a decrease in pyridinic nitrogen (N6) at the expense of both pyrrolic nitrogen (N5) and quaternary nitrogen (QN). It is noteworthy that for all carbons, the sum of both pyridinic and pyrrolic N was substantially greater than quaternary nitrogen. This fact could be, a priori beneficial from an electrochemical perspective, as the former two have a strong affinity toward Na ions due to their electron-deficient nature [64].

3.3. Electrochemical performance

3.3.1. Performance in NaTFSI/EC:DMC

In this section, the electrochemical performance of the HCs was assessed using the NaTFSI/EC:DMC electrolyte, a composite electrolyte featuring an ester-type solvent, which is the current industry standard in battery technology. Fig. 4 shows the first five galvanostatic discharge-charge cycles at a current density of 0.1 A g^{-1} for all the produced HCs. In line with the literature, all the profiles showed a slope region mainly associated with surface processes (from 2.5 to ca. 0.1 V) and a plateau region mainly ascribed to filling-pore and some intercalation phenomena (from ca. 0.1 to 0.01 V). The increase in carbonization temperature and enhanced ordering of the resulting carbons and reduction of surface defects, led to an improvement in initial coulombic efficiency (ICE), with values of 56.1 %, 70.6 %, and 79.4 % for HTC-800, HTC-1000, and HTC-1200 samples, respectively. Concerning the charge capacity measured in the 5th cycle, while the transition from 800 to 1000 °C resulted in an increase from 148.5 to 235.6 mAh g^{-1}, further heating to 1200 °C yielded a similar capacity of 233.0 mAh g^{-1}. At this relatively high temperature, although it increased the capacity associated with the plateau (see Fig. 4i), it also entailed a loss of reversible capacity attributed to the adsorption of Na ions on functional groups and defects. For their part, the carbons synthesized in the presence of pig manure exhibited slightly higher capacities and an analogous temperature-dependent behavior (see Fig. 4d–f), with values of 167.1 mAh g^{-1} (ICE = 60.4 %), 248.6 mAh g^{-1} (ICE = 71.5 %), and 259.4 mAh g^{-1} (ICE = 76.3 %) for HTC_{man}-800, HTC_{man}-1000, and HTC_{man}-1200,

Table 2
Structural parameters of HCs deduced from XRD and Raman spectroscopy.

	From XRD				From Raman	
	d_{002} [nm]	L_c [nm]	L_a [nm]	n	A_{D1}/A_G	L_a [nm]
HTC-800	0.385	0.887	2.875	2.305	8.053 ± 0.037	2.387 ± 0.011
HTC-1000	0.381	0.874	3.822	2.294	5.689 ± 0.225	3.379 ± 0.135
HTC-1200	0.379	0.913	4.303	2.407	4.350 ± 0.183	4.419 ± 0.186
HTC-1000ac	0.381	0.955	3.653	2.510	5.232 ± 0.325	3.675 ± 0.223
HTC_{man}-800	0.383	0.872	3.068	2.276	8.854 ± 0.526	2.171 ± 0.133
HTC_{man}-1000	0.378	0.934	3.612	2.473	5.518 ± 0.282	3.484 ± 0.175
HTC_{man}-1200	0.379	0.916	4.826	2.415	4.433 ± 0.286	4.337 ± 0.271
HTC_{man}-1000ac	0.380	0.924	3.470	2.428	5.801 ± 0.675	3.314 ± 0.412

Table 3
Surface areas and micropore volumes of HCs deduced from CO_2 and N_2 adsorption isotherms.

	Surface area BET [$m^2\ g^{-1}$]		Surface area NLDFT [$m^2\ g^{-1}$]		Pore volume NLDFT [$cm^3\ g^{-1}$]		
	N_2	CO_2	N_2	CO_2	V_{ultra}	V_{mic}	V_{mes}
HTC-800	82	397	59	602	0.122	0.080	0.025
HTC-1000	17	445	15	634	0.127	0.062	0.030
HTC-1200	17	52	14	43	0.005	0.014	0.032
HTC-1000ac	125	450	105	658	0.132	0.094	0.152
HTC_{man}-800	139	434	94	657	0.130	0.110	0.024
HTC_{man}-1000	23	370	18	533	0.102	0.072	0.033
HTC_{man}-1200	13	34	11	28	0.004	0.008	0.027
HTC_{man}-1000ac	110	452	92	655	0.128	0.094	0.132

respectively. Finally, the use of hydrochloric acid during the hydrothermal process resulted in a lower ICE, as well as a decrease in the capacity of the cycled electrode, yielding values of 182.5 mAh g^{-1} (ICE = 57.7 %) for HTC-1000ac and 226.4 mAh g^{-1} (ICE = 53.3 %) for HTC_{man}-1000ac.

The acquired CV curves for HTC-1000, HTC-1000ac, HTC_{man}-1000, and HTC_{man}-1000ac are shown in Fig. S17. The two distinctive peaks emerging at approximately 0.01 V (cathodic) and 0.12−0.18 V (anodic) can be linked to the reversible insertion-extraction of Na ions within the graphite-like interlayers, as well as pore filling [65]. The current response observed at higher voltages, broad peak observed between 0.25 and 1.0 V, is commonly attributed to pseudocapacitive phenomena and adsorption at heteroatoms in the surface of amorphous carbon materials. The comparison between the first cathodic scan and the following ones evidences the presence of irreversible reduction processes associated with the solid electrolyte interphase (SEI) formation. Results shown in Fig. S17 evidences a higher irreversibility for HCs synthesized under acidic conditions (HTC-1000ac and HTC_{man}-1000ac). This explains their relatively low ICE values and is consistent with their relatively high volume of mesopores, where ester-based electrolytes can infiltrate, react, and promote the formation of decomposition products building the SEI layers [66]. However, the nearly overlapped CV profiles obtained from the second cycle onwards seems to confirm the stability of the formed SEI for all the studied carbons.

To evaluate the rate capability of the HC-based electrodes, five discharge-charge cycles at various current densities (0.1, 0.5, 1, and 2 A g^{-1}) were conducted. As depicted in Fig. 5a, among the HTC-*x* carbons, the one produced at 1000 °C exhibited the best average rate performance, displaying reversible charging capacities of 236, 101, 72, 50, and 229 mAh g^{-1} when cycled at 0.1, 0.5, 1, 2, and again 0.1 A g^{-1}, respectively (see all measured capacities in Tables S2 and S3). At 0.1 A g^{-1}, the behavior of HTC-1000 was similar to that of HTC-1200, while at higher current rates, it reached specific capacities similar to those measured for HTC-800. This could be explained by HTC-1000 having appropriate features to ensure high contributions from the slope and plateau regions. For the slope region, its relatively developed micro- and ultra-microporosity, which was mostly generated during hydrothermal pretreatment, can enhance the diffusion of Na ions to the active storage sites. For the plateau region, its sufficient degree of ordering and the availability of a number of closed pores (see turbostratic closed void domains in Fig. 2b) can provide a satisfactory number of active sites for sodium accommodation. The favorable performance of HTC-1000 contrasts with the diffusion-related issues observed in our previous study for a VS-derived HC produced solely by pyrolytic treatment at 1000 °C, which showed considerably lower capacities of 91, 25, and 12 mAh g^{-1} at 0.1, 0.5, and 1 A g^{-1}, respectively [56].

When pig manure was used, the carbon produced at 1000 °C (HTC_{man}-1000) also demonstrated the best response across the applied currents, with charging capacities of 258, 97, 71, 44, and 242 mAh g^{-1} at 0.1, 0.5, 1, 2, and again 0.1 A g^{-1}, respectively (see Fig. 5b). The improvement in capacity observed at 0.1 A g^{-1}, in comparison with HTC-1000, could be attributed to the aforementioned heteroatom

Table 5
Functional groups quantification (at.%) from N 1s and S 2p XPS spectra regions.

	N 1s				S 2p		
	N6	N5	QN	N−O	C−S−C $S\ 2_{p3/2}$	C−S−C $S\ 2_{p1/2}$	C−SO_x−C
HTC-800	15.2	60.1	10.9	13.9	18.1	20.6	61.3
HTC-1000	14.2	65.7	13.4	8.61	25.8	18.8	55.4
HTC-1200	3.19	79.3	14.3	3.18	19.3	37.0	43.8
HTC-1000ac	12.9	66.9	12.8	7.44	–	–	–
HTC_{man}-800	28.0	49.3	18.9	3.80	29.1	14.4	56.5
HTC_{man}-1000	21.4	47.5	25.5	5.58	29.2	18.9	52.0
HTC_{man}-1200	3.37	53.4	38.1	5.11	47.7	23.7	28.7
HTC_{man}-1000ac	11.7	61.7	14.8	11.9	41.8	18.6	39.7

Table 4
Functional groups quantification (at.%) from C 1s and O 1s XPS spectra regions.

	C 1s				O 1s			
	sp^2C	sp^3C	C−O	C=O	C=O	C−O−C/COOH	C−O(H)	H_2O/O_2
HTC-800	48.6	21.4	15.6	14.4	48.1	43.6	3.79	4.52
HTC-1000	50.0	20.9	12.9	16.2	52.5	38.2	5.07	4.17
HTC-1200	52.1	17.7	11.0	19.3	67.4	20.4	11.5	0.76
HTC-1000ac	47.4	25.0	9.37	18.3	47.4	43.5	1.98	7.11
HTC_{man}-800	49.6	21.7	12.7	16.1	46.3	40.3	11.2	2.18
HTC_{man}-1000	50.6	21.9	11.4	16.1	48.4	38.4	7.55	5.62
HTC_{man}-1200	52.1	20.3	12.1	15.5	53.7	33.8	10.7	1.80
HTC_{man}-1000ac	45.2	23.8	14.2	16.8	49.9	39.9	3.57	6.66

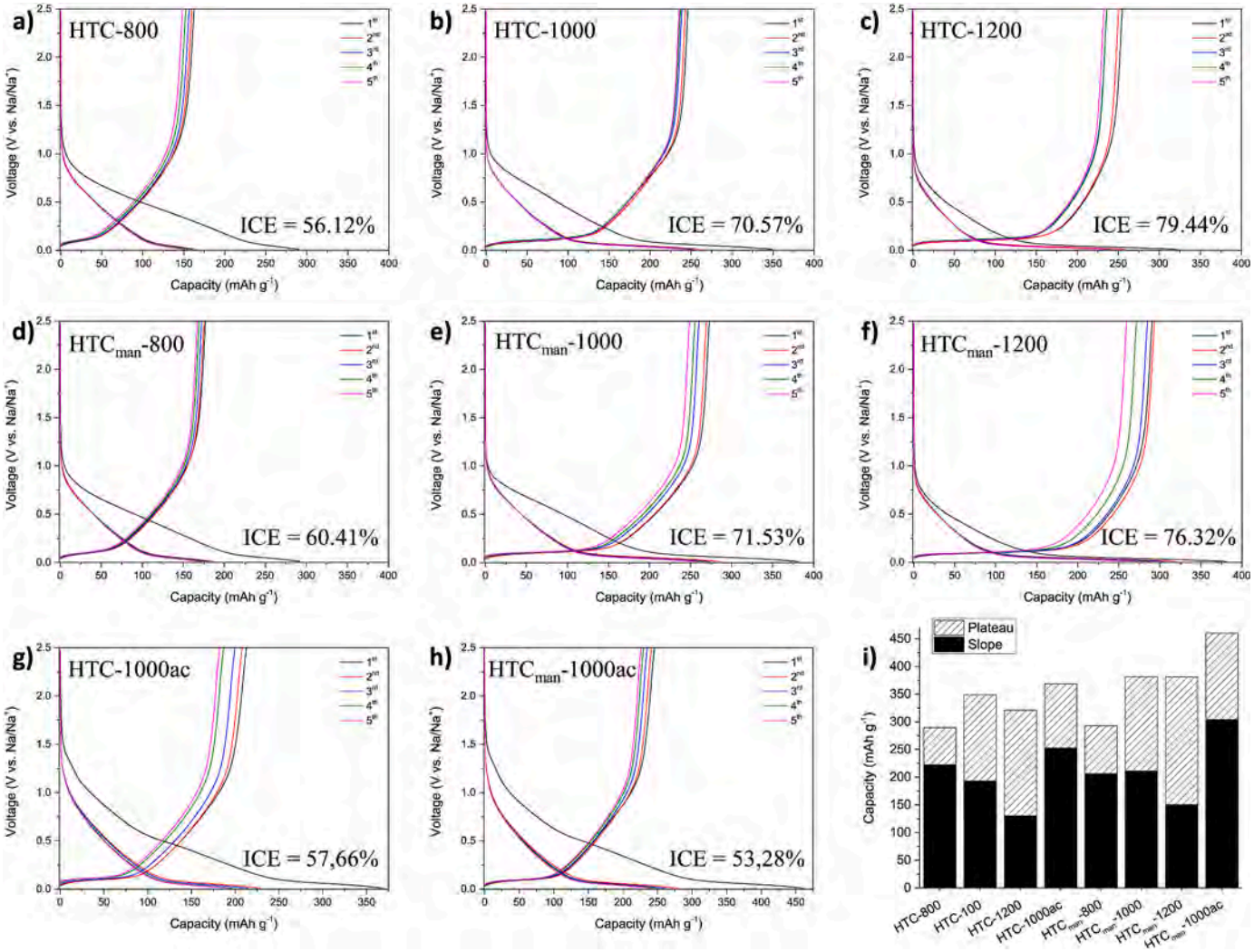

Fig. 4. Galvanostatic dis/charge profiles at a current rate of 0.1 Ag^{-1} for HTC-800 (a), HTC-1000 (b), HTC-1200 (c), HTC_{man}-800 (d), HTC_{man}-1000 (e), HTC_{man}-1200 (f), HTC-1000ac (g), and HTC_{man}-1000ac (h). Plateau and slope region contribution during the 1st sodiation (i).

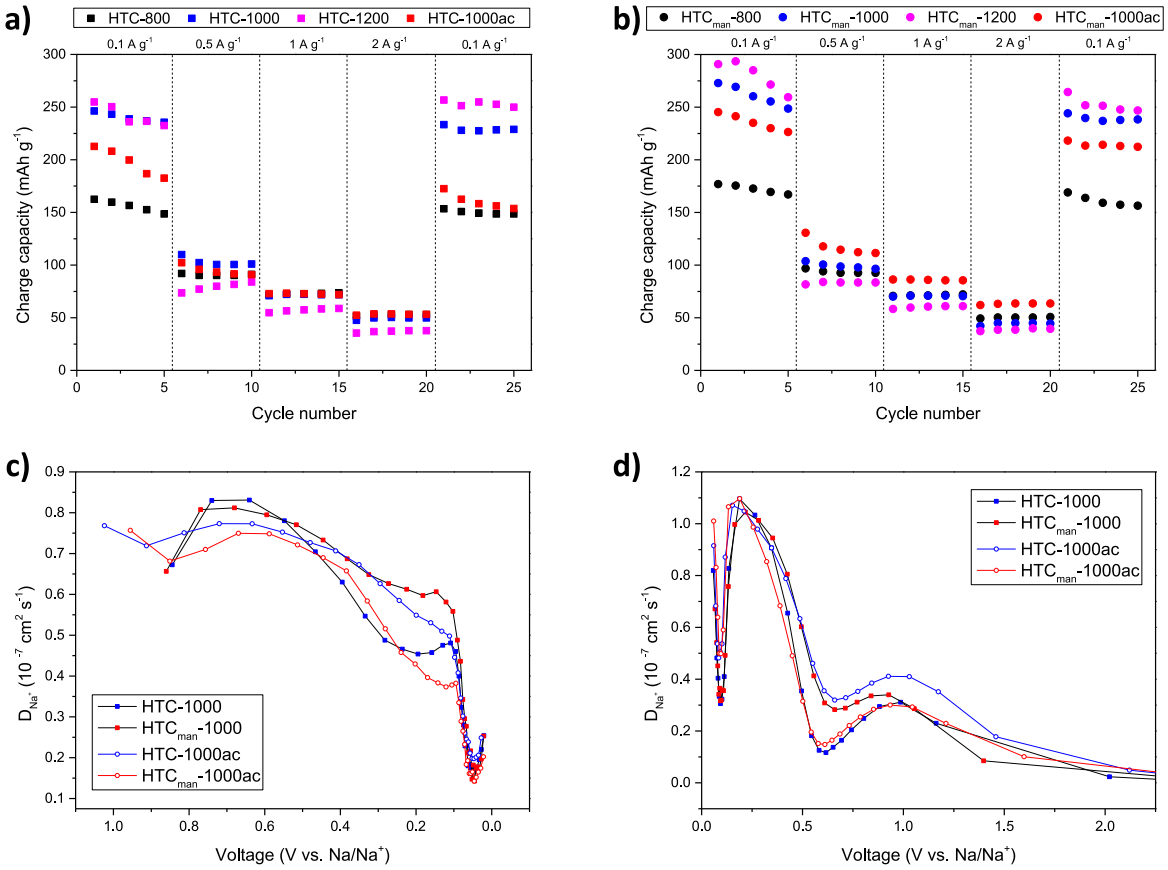

Fig. 5. Charge specific capacities at various current densities ranging from 0.1 to 2 A g^{-1} (a–b), and $D_{Na}{}^{+}$ values calculated from GITT measurements along sodiation (c) and desodiation (d).

doping (mainly N) of the carbon matrix. Furthermore, the addition of HCl during the hydrothermal pretreatment further improved the rate capability, due to the morphological changes discussed above, with special emphasis on the availability of microsphere clusters, capable of facilitating diffusion of Na ions during discharge and charge. The HTC_{man}-1000ac-based electrode delivered capacities of 226, 111, 86, 64, and 212 mAh g^{-1} at 0.1, 0.5, 1, 2, and again 0.1 A g^{-1}, respectively. Unfortunately, the capacity delivered at 0.1 A g^{-1} decreased by 12.4 % compared to that of HTC_{man}-1000. The reduced capacity can be associated with a more resistive SEI formed at the electrode surface, associated with the large amount of decomposition during the first sodiation, leading to a relatively low ICE of 53.3 % for HTC_{man}-1000ac (see Fig. 4).

Fig. 5c and d shows the apparent diffusion coefficients (D_{Na}^{+}) calculated from GITT data for both sodiation and desodiation processes. The working electrode underwent a preconditioning step of 5 CV scans at 0.1 mV s^{-1} to facilitate the formation and stabilization of the SEI. The initial faster stage during sodiation occurring above 0.1 V is primarily attributed to the adsorption of Na ions on the surface and structural defects. As all these storage sites are gradually occupied, Na ions begin to intercalate into the graphite-like interlayers. Since Na ions must overcome the strong energy barrier from graphitic sheets, the $D_{Na}{}^{+}$ values dramatically decreased at the beginning of the plateau stage (≈0.1 V). During this second stage, pore filling (of both open micro- and ultra-micropores and closed pores) also coexists with intercalation, as recently reported by Yin et al. in an excellent study [67]. Finally, the increase in diffusivity observed at ca. 0.05 V (third stage) can be ascribed to a certain sodium plating in the filled pores [68]. As can be deduced from Fig. 5c and d, all HCs showed the same kinetic behavior according to the three-stage mechanism explained above.

To assess the cycling stability of the HCs-derived anodes synthesized at 1000 °C, 250 discharge-charge cycles at 1 A g^{-1} were conducted following an initial set of 5 cycles at 0.1 A g^{-1}. Surprisingly, the utilization of pig manure during the hydrothermal stage improved the cycling stability of the resulting carbons, leading to an increase in capacity retention (i.e., percentage of the initial capacity at 0.1 A g^{-1} measured at the same current rate after 250 cycles at 1 A g^{-1}) from 77 % for HTC-1000 to 92 % for HTC_{man}-1000 (see Fig. 6). Similarly, HTC_{man}-1000ac also exhibited a significant improvement in capacity retention with respect to that observed for HTC-1000ac (from 61 % to 81 %). In light of these results, we hypothesize that carbon fragments derived from the organic matter contained in the pig manure might play a stabilizing role within the primary carbonaceous matrix. These manure-derived carbon forms, synthesized in situ on the VS-derived carbon, can act as a binder, enhancing the structural stability and thereby minimizing the segregation of carbonaceous particles resulting from volumetric changes associated to sodiation-desodiation processes. Doping with nitrogen heteroatoms also enhances the electrical conductivity of the HC and reinforces its structural stability through the reduction in volume expansion upon sodiation [69,70]. Furthermore, the presence of well-ordered domains with interlayer distances below 0.3 nm can endow the overall structure with larger stability, since they can act as scaffolds to accommodate volume changes.

3.3.2. *Performance of the best-performing HCs in different electrolytes*

The electrochemical performance of both HTC_{man}-1000 and HTC_{man}-1000ac—the most attractive hard carbons analyzed—were characterized employing different ether- and ester-based electrolytes. As a preliminary step, the respective electrodes were prepared using Na-CMC as the sole binder (10 wt% in the resulting slurry) in order to determine the suitability of employing SBR as co-binder. The use of SBR in

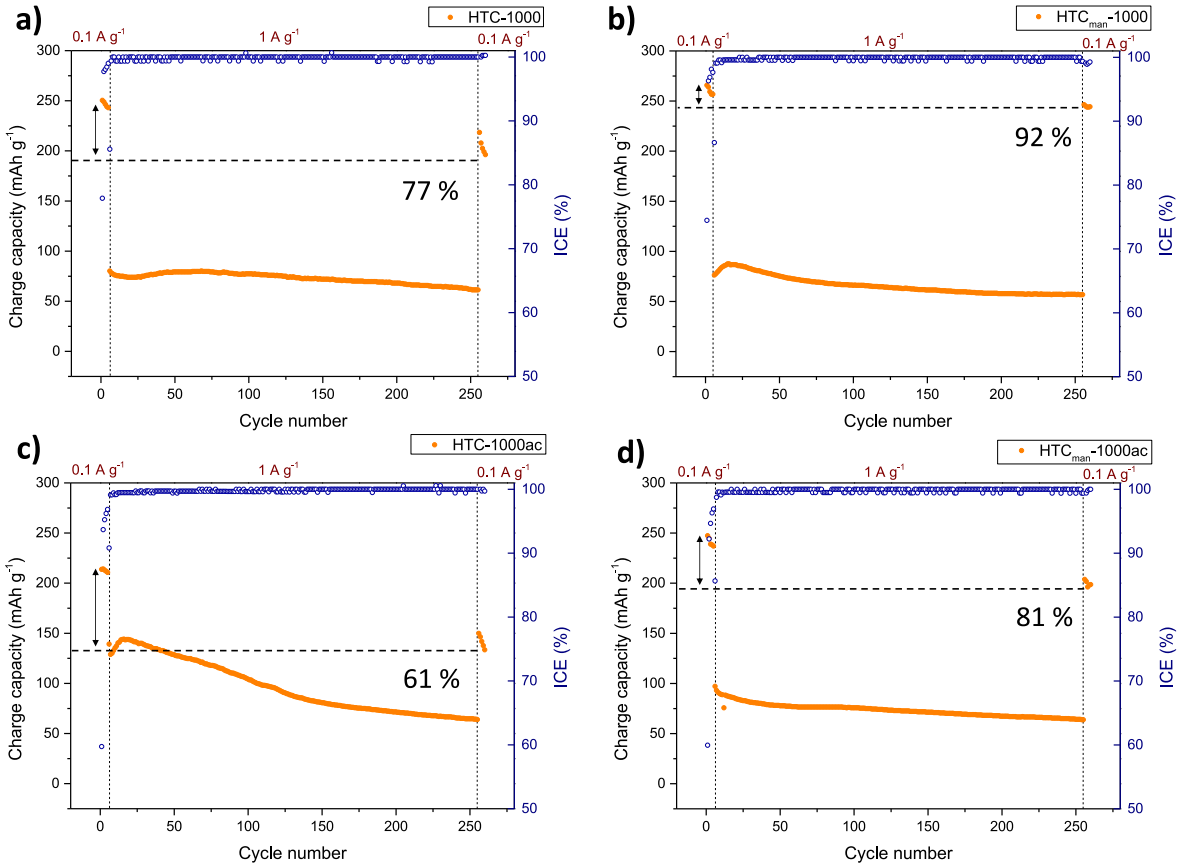

Fig. 6. Cycling performance of HTC-1000 (a), HTC_{man}-1000 (b), HTC-1000ac (c), and HTC_{man}-1000ac (d) for the following sequence: 5 cycles at 0.1 A g^{-1} plus 250 cycles at 1 A g^{-1} plus 5 cycles at 0.1 A g^{-1}.

combination with Na-CMC is widely acknowledged to enhance the flexibility and adhesion of high loading-electrode coatings. Nonetheless, an excess of the elastomer (employed to mitigate the brittleness of Na-CMC) can lead to a decrease in both the electronic conductivity and porosity of the electrode [71,72]. In this respect, Fig. S18 illustrates how the use of pure Na-CMC as binder improved the rate capability of both HTC_{man}-1000- and HTC_{man}-1000ac-based electrodes. Therefore, this binder was chosen for subsequent experiments in the study.

Glyme-based electrolytes have gained prominence for their ability to facilitate the intercalation of solvated sodium ions into graphite anodes through the reversible "co-intercalation mechanism." Moreover, when used with HC electrodes, ether-based electrolytes produce thinner and more compact, stable, and ion-conducting SEI layers than ester-based electrolytes, which a priori should enhance the electrochemical behavior of HC electrodes [73]. To verify the aforementioned assertion, HTC_{man}-1000 and HTC_{man}-1000ac anodes were cycled at different intensities using four new electrolytes—$NaPF_6$ or NaFSI salts in EC:DMC or diglyme (DGM) solvents—in addition to the previously used NaTFSI/EC:DMC.

From the GCD measurements over the first 5 cycles at 0.1 A g^{-1}, which are illustrated in Figs. S19 and S20, it can be deduced that the $NaPF_6$/DGM electrolyte exhibited the best performance in terms of coulombic efficiency and storage capacity, with reversible capacities of 227 and 239 mAh g^{-1} for HTC_{man}-1000 and HTC_{man}-1000ac, respectively. In addition, using the diglyme solvent also resulted in an improvement in the ICE of HTC_{man}-1000ac (see Fig. S21), which gradually increased from 46.4 % (NaFSI), 53.3 % ($NaPF_6$), and 62.9 % (NaTFSI) in the EC:DMC solvent, to 72.9 % in the $NaPF_6$/DGM electrolyte. Nonetheless, the use of NaFSI salt in the DGM solvent resulted in a modest ICE of 61.0 % (for HTC_{man}-1000ac). In fact, the half-cell failed after the first 5 cycles, with erratic voltage profiles observed during the desodiation process (for both HTC_{man}-1000 and HTC_{man}-1000ac, as shown in Fig. S22). These results are consistent with what was observed by Goktas et al. [74] for graphite anodes, where the use of NaFSI and NaTFSI in diglyme led to exfoliation and delamination phenomena of the carbonaceous electrode because of continuous side reactions with the electrolyte, in addition to a more resistive interphase on the metallic sodium counter electrode.

Table 6
Atomic percentage from the survey XPS spectra of HTC_{man}-1000ac electrode cycled in different electrolytes.

	C 1s	O 1s	Na 1s	F 1s	S
Pristine	72.6	22.1	4.6	0.7	–
NaFSI/DGM	49.7	29.9	14.4	3.4	2.6
$NaPF_6$/DGM	53.9	31.9	13.1	1.1	–
$NaPF_6$/EC:DMC	47.5	35.9	13.2	3.4	–

In order to check the influence of the electrolyte on the electrode surface, SEM images of the HTC_{man}-1000ac-based electrode cycled in NaFSI/DGM, $NaPF_6$/DGM, and $NaPF_6$/EC:DMC electrolytes (during the rate capability tests of 40 cycles) were obtained (see Figs. S23–S25). From the images, it can be appreciated that significant differences existed between the electrode surface film with the ester (EC:DMC) and those formed with the ether (DGM). The former solvent, owing to its higher reactivity toward reduction, results in the formation of a porous film at the electrode surface with a rough morphology, featuring areas where degradation compounds were accumulated leading to the formation of semi-spherical complexes (see Fig. S23d). It is important to note that the filaments observed in some images correspond to remnants

Table 7
Contributions (at. %) of the different peaks from deconvoluted C 1s, O 1s, and F 1s XPS spectra regions of HTC_{man}-1000ac electrode cycled in different electrolytes.

	C 1s				O 1s			F 1s	
	C—C /C—H	C—O	C=O	Na—HC	Na—O /C=O	O—C /O—H	O—C=O /O—F	Na—F	P—F
Pristine	49.1	42.8	8.08	–	15.2	56.5	28.4	–	–
NaFSI/DGM	74.7	11.5	10.4	3.45	38.2	33.7	28.1	100	–
$NaPF_6$/DGM	69.4	14.9	14.9	1.79	44.1	32.6	23.3	22.5	77.5
$NaPF_6$/EC:DMC	1.90	56.4	20.7	21.0	38.9	39.8	21.3	3.01	97.0

of the fiberglass separator. Furthermore, although the substantial amount of product accumulated at the surface, the low quality of the passivation film leads to the formation of cracks and regions where the carbon was exposed (Fig. S26d), promoting increased electrolyte decomposition. In contrast, when DGM was employed as solvent, a relatively uniform and much thinner passivation film was formed, which was adhered to the surface of carbonaceous particles while maintaining porosity among them (see Figs. S24b and S24c). Regarding the use of NaFSI and $NaPF_6$ salts with DGM, upon examining images taken at higher magnification (Figs. S25b, S25c, S26b, and S26c), a more pronounced SEI layer was observed when NaFSI was used. In fact, the differences between the pristine electrode and that cycled in $NaPF_6$/DGM were almost imperceptible due to the low thickness of the formed SEI. This type of compact SEI, dense enough to prevent further electrolyte decomposition and able to facilitate rapid transport of Na ions, is behind the improved ICE and high-rate capability.

Since the formed SEI layer contains both organic and inorganic species resulting from the solvents and salt anions degradation, respectively [12], surface chemistry characterization of both pristine and cycled HTC_{man}-1000ac-based electrodes was conducted using XPS (see Figs. S27–S30 for obtained spectra). As can be deduced from Table 6, the contents on surface of F, Na, and O increased after cycling for all the electrolytes tested, suggesting the formation of SEI layers composed of both organic and inorganic compounds. For the ester-based electrolyte ($NaPF_6$/EC:DMC), the lowest C content was measured. This could be related to a higher extent of side reactions and the resulting formation of a thicker SEI layer rich in sodium alkyl carbonates [75].

The C 1s region of the pristine electrode was deconvoluted into three peaks corresponding to C—C and C—H bonds, C—O bonds, and C=O bonds at ca. 284.8, 286.1, and 288.6 eV, respectively. It should be noted that the sizeable C—O peak in the pristine material may result from the Na-CMC binder. For the cycled electrodes, a fourth peak assigned to the sodiated Na in the HC appeared at a low binding energy of 283.9 eV. The O1s peaks at ca. 530.6, 532.3, and 535.2 eV were assigned to Na—O/C=O, O—C/O—H, and O—C=O/O—F bonds, respectively, since the electrolyte salt reduction give rise to these Na—F and O—F inorganic bonds [76]. The same degradation reaction can also explain the P—F and Na—F peaks in the F1s spectra at 683 and 686 eV, respectively. The resulting surface composition of cycled electrodes, given in Table 7, revealed a notable shift in the nature of the SEI layer depending on the

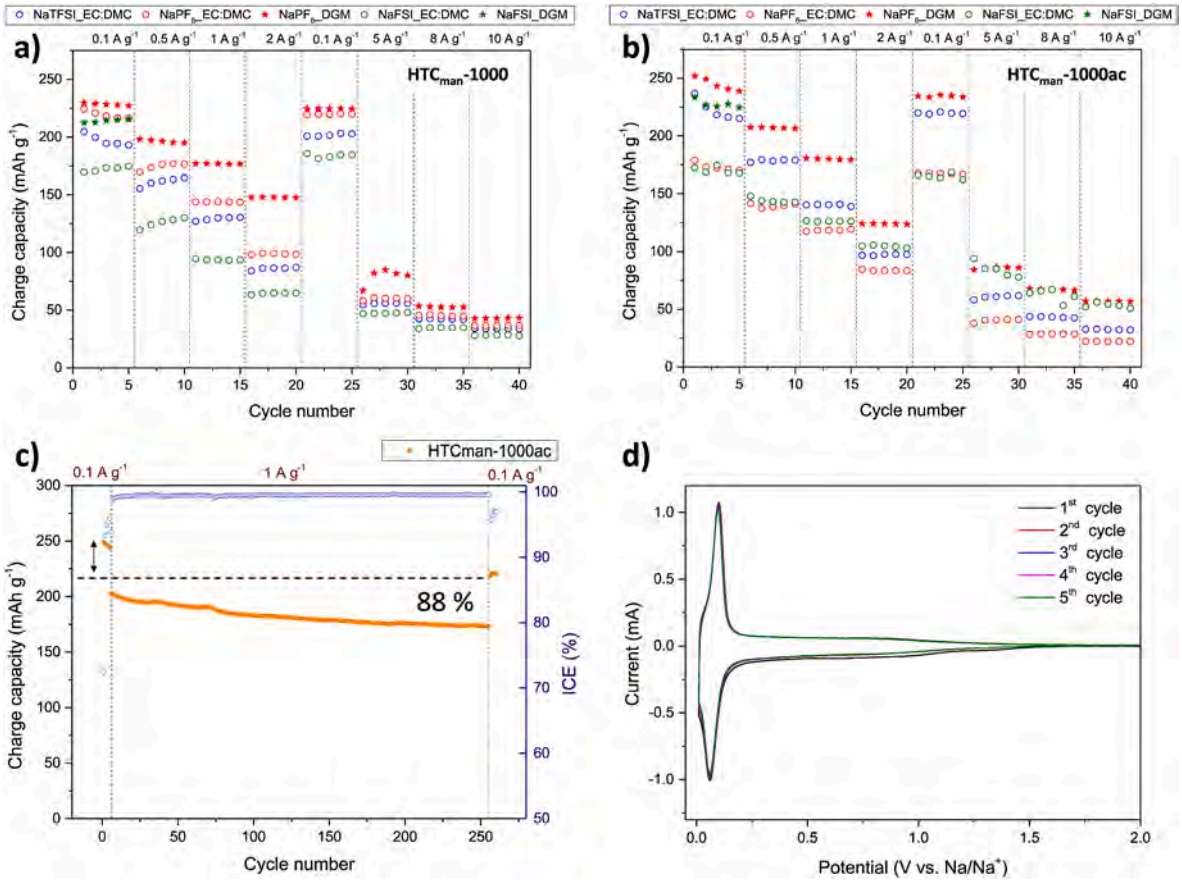

Fig. 7. Charge specific capacities at various current densities ranging from 0.1 to 10 A g^{-1} (a–b), cycling performance of HTC_{man}-1000ac for 250 cycles at 1 A g^{-1} in $NaPF_6$/DGM electrolyte (c), and CV curves of the first five cycles of HTC_{man}-1000ac cycled in $NaPF_6$/DGM electrolyte at 0.1 A g^{-1} (d).

type of solvent employed in the electrolyte, namely ether or ester. When employing the EC:DMC electrolyte, the C—C peak was almost undetectable, suggesting a SEI thickness close to the depth reachable by XPS analysis (approximately 10 nm). Additionally, the higher proportion of unstable C—O organic groups was probably attributed to the electrochemically-induced ring opening of EC, leading to the formation of polyethylene oxide (PEO) oligomeric/polymeric species and the release of CO_2 [77]. On the other hand, the increased C—C/C—H peaks observed for the SEI layers when $NaPF_6$/DGM and NaFSI/DGM solvents were used are consistent with the primary reduction products of diglyme sodium alkoxides (RCH_2ONa), whereas the decomposition of esters yields sodium alkyl carbonate ($ROCO_2Na$) [78]. It has been reported that sodium alkoxides (RCH_2ONa) reduce the energy barrier for Na-ion diffusion and play a crucial role in interfacial stability. The utilization of diglyme also resulted in higher contents of NaF, which is highly impermeable to the electrolyte solvent (preventing SEI enlargement) and also exhibits relatively low activation energies for Na-ion diffusion [79].

Regarding the rate capability, the $NaPF_6$/DGM electrolyte also exhibited the best results (see Fig. 7a and b). Under these conditions, the HTC_{man}-1000ac material delivered specific capacities of 180, 86, and 57 mAh g^{-1} when cycled at 1, 5, and 10 A g^{-1} (see Tables S4 and S5). This substantial improvement in rate capability, compared to the results obtained using the NaTFSI/EC:DMC electrolyte, aligns with the recent findings reported by Yin et al. [80] and can be ascribed to an enhanced diffusion rate and charge-transfer kinetics (thinner SEI layer), as well as to a lower SEI resistance and desolvation energy. Capacity retention was also improved, as depicted in Fig. 7c, showcasing a retention rate of 88 % after 250 cycles, surpassing the 81 % achieved using the NaTFSI/EC:DMC electrolyte (see Fig. 6d). The CV curves plotted in Fig. 7d also corroborated the formation of a thinner SEI with low irreversibility and very high stability when the HTC_{man}-1000ac-based electrode was cycled in $NaPF_6$/DGM. Compared to other HCs synthesized via HTC of lignocellulosic wastes reported in the literature (see Table S6), both HTC_{man}_1000 and HTC_{man}_1000ac perform outstanding results. They excel notably in terms of rate capability, achieving capacities at current densities of 1 A g^{-1} that surpass those obtained in studies where activating agents and dopants were used during the HTC. This highlights the advantages of using pig manure as the hydrothermal solvent, resulting in hard carbons with rate performances comparable to those recently achieved from synthetic organic-derived HCs [81,82].

To better clarify the interfacial behavior of electrodes, EIS measurements were performed after the first and tenth cycles for both HTC_{man}-1000 and HTC_{man}-1000 electrodes in the $NaPF_6$/DGM electrolyte (see Fig. S31 for the corresponding Nyquist plots). The impedance data reveal consistent features: (i) a semicircle at high frequencies corresponding to ion migration through the passivation layer, partially overlapping with (ii) a semicircle at mid frequencies related to the interfacial charge-transfer process; and (iii) a sloped line at low frequencies indicating Na^+ ion diffusion in the bulk of the active materials. EIS data were fitted to an equivalent circuit model described by Boukamp's notation as R_{sol} (R_{SEI} C_{SEI}) ($R_{CT}C_{DL}$)WC_i. This model includes R_{sol} for the Na-ion resistance in the electrolyte, R_{SEI} and C_{SEI} for the resistance and capacitance of the solid electrolyte interphase, R_{CT} and C_{DL} for the charge-transfer resistance and double-layer capacitance, Warburg diffusion (W) for solid-state Na-ion diffusion, and C_i for differential intercalation [83]. Due to the electrode surface roughness, all capacitance elements (C) were substituted with constant-phase elements (Q). The overall impedance values for HTC_{man}-1000ac are slightly lower than those for HTC_{man}-1000 after both the 1st and the 10th cycles, as

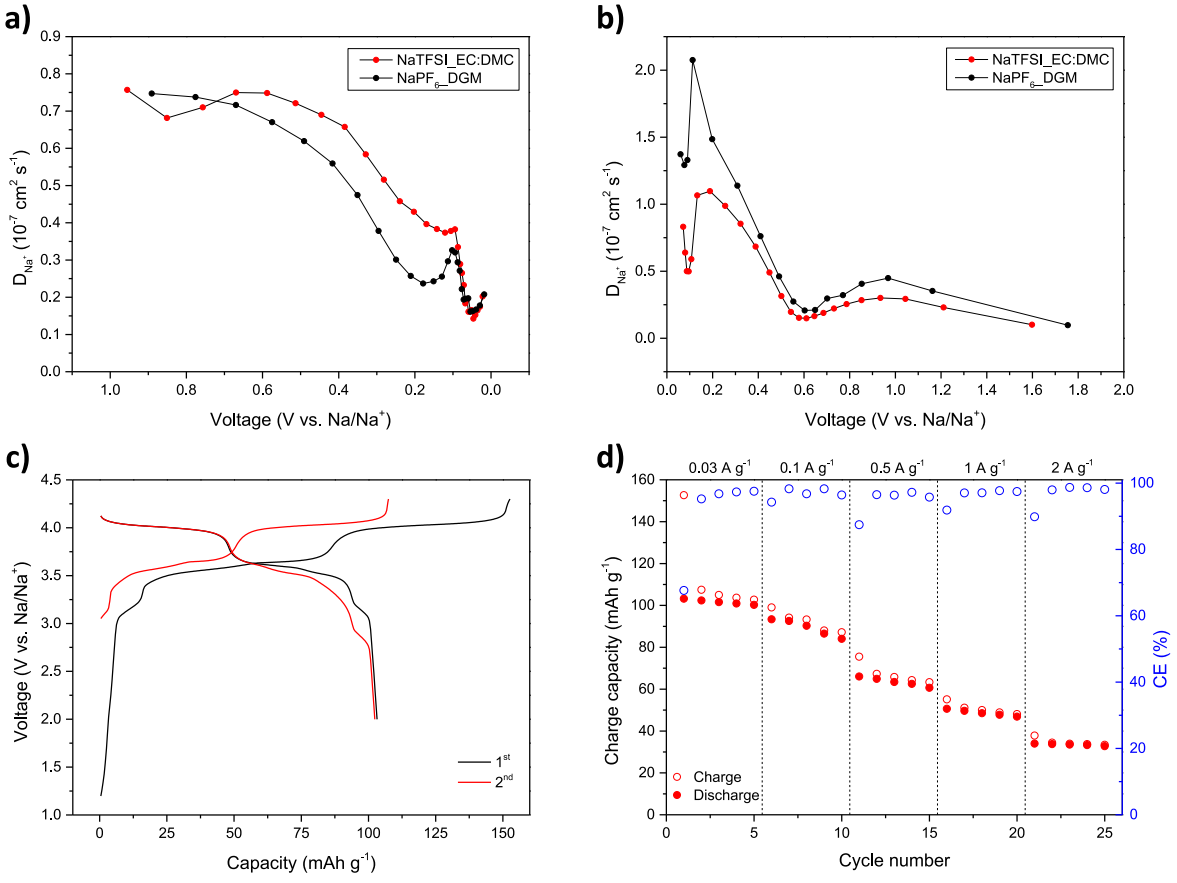

Fig. 8. D_{Na^+} values calculated from GITT measurements of HTC_{man}-1000ac half cells in NaTFSI/EC:DMC and $NaPF_6$/DGM electrolytes along sodiation (a) and desodiation (b). Galvanostatic discharge-charge profiles at 0.03 A g^{-1} (c) and rate performance (d) of the NVPF/HTC_{man}-1000ac full-cell.

expected due to the higher porosity of the HTC_{man}-1000ac carbon (Table S7). The subsequent reduction in R_{CT} and R_{SEI} observed in both anodes after 10 cycles is likely attributed to the reorganization of the electrode/electrolyte interface, which is induced by initial morphological instability [84].

Fig. 8 compares the apparent diffusion coefficients (D^{+}_{Na}) acquired through GITT for the HTC_{man}-1000ac-based electrode in NaTFSI/EC:DMC and $NaPF_6$/DGM electrolytes. During sodiation (Fig. 8a), it can be observed that the use of DGM did not seem to kinetically improve the storage of Na ions through intercalation and pore filling, since $D_{Na}{}^{+}$ values were very similar in the low-voltage region. Nevertheless, a shift in the above-proposed three-stage mechanism seemed to occur at relatively high potential (i.e., above 0.1 V). The most plausible hypothesis would be the occurrence of intercalation of both Na ions and DGM-derived complexes into the graphite-like domains [85]. This co-intercalation phenomenon at the voltage range from 1 V to 0.1 V would be responsible for a lower diffusion coefficient compared to that observed using the EC:DMC-based electrolyte, since in the latter case, the apparent diffusion coefficients were exclusively associated to faster surface adsorption phenomena [86]. It should also be highlighted the relatively high diffusion coefficients obtained during the entire desodiation process when the EC:DMC-based electrolyte was replaced by the DGM-based one.

To further demonstrate the practical implementation of the anode material developed in the present study, full cells were assembled pairing a $Na_3V_2(PO_4)2F_3$ (NVPF) cathode with the HTC_{man}-1000ac anode and using $NaPF_6$ in DGM as electrolyte. The charge curves (Fig. 8c) showed two main voltage plateaus at ~3.6 V and at ~4 V related with V^{3+}/V^{4+} redox and the subsequent two Na ion extractions from NVPF. During the second cycle, the full cell delivered a reversible capacity of 102 mAh $g^{-1}_{cathode}$. Considering a nominal potential of 3.7 V, the full cell delivered a noteworthy energy density of 274.7 W h kg^{-1} (based on the total mass of the active materials in the cathode and anode), making this kind of anode/cathode/electrolyte combination attractive for further research and coupling optimization.

4. Conclusions

This study has proven the potential of pig manure as a suitable hydrothermal medium to synthesize high-performance anodes for SIBs. Thus, its direct valorization as HTC solvent without the need for any pretreatment and/or drying appears as a very attractive option from an energy, environmental, and economic standpoint. Regarding the carbonization of the plant biomass (vine shoots), it has been demonstrated that a hydrothermal pretreatment significantly enhanced the properties of the resulting hard carbon, especially in terms of connected micro- and ultra-microporous networks, which facilitate the diffusion of Na ions within the active material and also provide additional storage sites in the plateau region. Furthermore, the addition of HCl during the hydrothermal step has also proven effective in inducing beneficial changes in the carbon structure, such as a certain development of mesopores and the formation of microsphere clusters. The proposed synthesis route for producing low-cost and high-performance hard carbons could serve as an effective strategy to valorize the mentioned agronomic residues and could be easily extended for industrial applications.

Concerning the electrochemical performance, it has been observed that the addition of SBR as a binder may negatively impact the performance of the anode. In terms of the electrolyte, it is noteworthy that the hard carbons produced in the present study exhibited superior electrochemical performance in ether (DGM) compared to ester (EC:DMC) in terms of ICE, cycling stability, and rate capability. The use of DGM, thanks to the formation of a thinner and a more permeable and stable SEI, paves the way for employing HCs with greater porosity and, consequently, improved kinetics. The interactions among all these elements (i.e., active materials, binder, salts, and electrolyte solvents) must be further considered for a systematic study that enables the development of optimized carbonaceous anodes tailored to the specific system.

CRediT authorship contribution statement

Darío Alvira: Writing – original draft, Methodology, Investigation. **Daniel Antorán:** Investigation. **Hamideh Darjazi:** Methodology, Investigation. **Giuseppe Antonio Elia:** Supervision, Conceptualization. **Victor Sebastian:** Supervision, Investigation, Conceptualization. **Joan J. Manyà:** Writing – review & editing, Supervision, Funding acquisition, Conceptualization.

Declaration of competing interest

The authors declare that they have no known competing financial interests or personal relationships that could have appeared to influence the work reported in this paper.

Data availability

Data will be made available on request.

Acknowledgments

This work is part of the research project PID2019-107737RB-I00, funded by MCIN/AEI/10.13039/501100011033 and "ERDF A way of making Europe". VS acknowledge funding from project PID2021-127847OB-I00 MCIN/AEI/10.130 and PDC2022-133866-I00 MCIN/AEI/10.13039/501100011033. The authors also acknowledge the funding from the Aragon Government (Ref. T22_23R). DA also acknowledges the funding from the Regional Government of Aragon (Spain) with a grant for postgraduate research contracts (2019–2023). LMA-ELECMI and NANBIOSIS ICTs are gratefully acknowledged.

Appendix A. Supplementary data

Supplementary data to this article can be found online at https://doi.org/10.1016/j.jpowsour.2024.235043.

References

[1] F. Trotta, G.J. Wang, Z. Guo, Z. Xu, M. Crespo Ribadeneyra, H. Au, J.S. Edge, M. M. Titirici, L. Lander, A comparative Techno-economic and lifecycle analysis of biomass-derived anode materials for Lithium- and sodium-ion batteries, Adv. Sustain. Syst. 6 (2022) 2200047, https://doi.org/10.1002/adsu.202200047.
[2] M. Thompson, Q. Xia, Z. Hu, X.S. Zhao, A review on biomass-derived hard carbon materials for sodium-ion batteries, Mater. Adv. 2 (2021) 5881–5905, https://doi.org/10.1039/D1MA00315A.
[3] W. Shao, H. Shi, X. Jian, Z.-S. Wu, F. Hu, Hard-carbon anodes for sodium-ion batteries: recent Status and challenging perspectives, Adv. Energy Sustain. Res. 3 (2022) 2200009, https://doi.org/10.1002/aesr.202200009.
[4] D. Alvira, D. Antorán, J.J. Manyà, Plant-derived hard carbon as anode for sodium-ion batteries: a comprehensive review to guide interdisciplinary research, Chem. Eng. J. 447 (2022) 137468, https://doi.org/10.1016/j.cej.2022.137468.
[5] L. Jiménez, V. Angulo, E. Ramos, M.J. De la Torre, J.L. Ferrer, Comparison of various pulping processes for producing pulp from vine shoots, Ind. Crops Prod. 23 (2006) 122–130, https://doi.org/10.1016/j.indcrop.2005.05.001.
[6] J. Zhu, Y. Shan, T. Wang, H. Sun, Z. Zhao, L. Mei, Z. Fan, Z. Xu, I. Shakir, Y. Huang, B. Lu, X. Duan, A hyperaccumulation pathway to three-dimensional hierarchical porous nanocomposites for highly robust high-power electrodes, Nat. Commun. 7 (2016) 13432, https://doi.org/10.1038/ncomms13432.
[7] D. Qin, S. Chen, A sustainable synthesis of biomass carbon sheets as excellent performance sodium ion batteries anode, J. Solid State Electrochem. 21 (2017) 1305–1312, https://doi.org/10.1007/s10008-016-3485-z.
[8] P. Yu, W. Tang, F.-F. Wu, C. Zhang, H.-Y. Luo, H. Liu, Z.-G. Wang, Recent progress in plant-derived hard carbon anode materials for sodium-ion batteries: a review, Rare Met. 39 (2020) 1019–1033, https://doi.org/10.1007/s12598-020-01443-z.
[9] A. Funke, F. Ziegler, Hydrothermal carbonization of biomass: a summary and discussion of chemical mechanisms for process engineering, Biofuels, Bioprod. Biorefining 4 (2010) 160–177, https://doi.org/10.1002/bbb.198.
[10] P. Zheng, T. Liu, X. Yuan, L. Zhang, Y. Liu, J. Huang, S. Guo, Enhanced performance by enlarged Nano-pores of Holly Leaf-derived lamellar carbon for

sodium-ion battery anode, Sci. Rep. 6 (2016) 26246, https://doi.org/10.1038/srep26246.
[11] J. Wang, L. Yan, Q. Ren, L. Fan, F. Zhang, Z. Shi, Facile hydrothermal treatment route of reed straw-derived hard carbon for high performance sodium ion battery, Electrochim. Acta 291 (2018) 188–196, https://doi.org/10.1016/j.electacta.2018.08.136.
[12] G.G. Eshetu, T. Diemant, M. Hekmatfar, S. Grugeon, R.J. Behm, S. Laruelle, M. Armand, S. Passerini, Impact of the electrolyte salt anion on the solid electrolyte interphase formation in sodium ion batteries, Nano Energy 55 (2019) 327–340, https://doi.org/10.1016/j.nanoen.2018.10.040.
[13] E. García-Bordejé, E. Pires, J.M. Fraile, Parametric study of the hydrothermal carbonization of cellulose and effect of acidic conditions, Carbon N. Y. 123 (2017) 421–432, https://doi.org/10.1016/j.carbon.2017.07.085.
[14] J. Köninger, E. Lugato, P. Panagos, M. Kochupillai, A. Orgiazzi, M.J.I. Briones, Manure management and soil biodiversity: towards more sustainable food systems in the EU, Agric. Syst. 194 (2021) 103251, https://doi.org/10.1016/j.agsy.2021.103251.
[15] Eurostat, Agri-environmental indicator - livestock patterns. https://ec.europa.eu/eurostat/statistics-explained/index.php?title=Agri-environmental_indicator_-_livestock_patterns#Focus_on_the_agricultural_holdings_with_livestock_in_2016, 2019.
[16] G. Pexas, S.G. Mackenzie, M. Wallace, I. Kyriazakis, Environmental impacts of housing conditions and manure management in European pig production systems through a life cycle perspective: a case study in Denmark, J. Clean. Prod. 253 (2020) 120005, https://doi.org/10.1016/j.jclepro.2020.120005.
[17] W. Antezana, C. De Blas, P. García-Rebollar, C. Rodríguez, A. Beccaccia, P. Ferrer, A. Cerisuelo, V. Moset, F. Estellés, M. Cambra-López, S. Calvet, Composition, potential emissions and agricultural value of pig slurry from Spanish commercial farms, Nutrient Cycl. Agroecosyst. 104 (2016) 159–173, https://doi.org/10.1007/s10705-016-9764-3.
[18] Z. Tu, J. Shui, J. Liu, H. Tuo, H. Zhang, C. Lin, J. Feng, Y. Feng, W. Su, A. Zhang, Exploring the abundance and influencing factors of antimicrobial resistance genes in manure plasmidome from swine farms, J. Environ. Sci. 124 (2023) 462–471, https://doi.org/10.1016/j.jes.2021.11.030.
[19] P. Martins-Silva, C. de P. Dias, L.C. Vilar, S. de Queiroz Silva, C.C. Rossi, M. Giambiagi-deMarval, Dispersion and persistence of antimicrobial resistance genes among Staphylococcus spp. and Mammaliicoccus spp. isolated along a swine manure treatment plant, Environ. Sci. Pollut. Res. (2022) 34709–34719, https://doi.org/10.1007/s11356-022-24725-8.
[20] T. Chen, M. Zhao, X. Tang, W. Wang, M. Zhang, J. Tang, W. Wang, W. Wei, B. Ma, Y. Zou, N. Zhang, J. Mi, Y. Wang, X. Liao, Y. Wu, Serious risk of tigecycline resistance in Escherichia coli isolated from swine manure, Microb. Ecol. (2022), https://doi.org/10.1007/s00248-022-02133-2.
[21] M.E. Ramírez-Islas, L.P. Güereca, F.S. Sosa-Rodriguez, M.A. Cobos-Peralta, Environmental assessment of energy production from anaerobic digestion of pig manure at medium-scale using life cycle assessment, Waste Manag. 102 (2020) 85–96, https://doi.org/10.1016/j.wasman.2019.10.012.
[22] H. Zheng, F. Tang, Y. Lin, Z. Xu, Z. Xie, J. Tian, Solid-state anaerobic digestion of rice straw pretreated with swine manure digested effluent, J. Clean. Prod. 348 (2022) 131252, https://doi.org/10.1016/j.jclepro.2022.131252.
[23] W. Zhang, B. Xiao, K. Zhang, H. Chen, X. Guo, Effects of mixing ratios on anaerobic co-digestion of swine manure and rice straw: methane production and kinetics, Biomass Convers. Biorefinery (2021) 1553–1563, https://doi.org/10.1007/s13399-020-01211-0.
[24] V. Molina-Moreno, J. Leyva-Díaz, F. Llorens-Montes, F. Cortés-García, Design of indicators of circular economy as instruments for the evaluation of sustainability and efficiency in wastewater from pig farming industry, Water 9 (2017) 653, https://doi.org/10.3390/w9090653.
[25] I. González-García, B. Riaño, B. Molinuevo-Salces, M.B. Vanotti, M.C. García-González, Improved anaerobic digestion of swine manure by simultaneous ammonia recovery using gas-permeable membranes, Water Res. 190 (2021) 116789, https://doi.org/10.1016/j.watres.2020.116789.
[26] F. Zhu, C. Hong, W. Wang, H. Lyu, W. Zhu, H. Xv, Y. Yao, A microbial agent effectively reduces ammonia volatilization and ensures good maggot yield from pig manure composted via housefly larvae cultivation, J. Clean. Prod. 270 (2020) 122373, https://doi.org/10.1016/j.jclepro.2020.122373.
[27] M. Jiao, X. Ren, Y. He, J. Wang, C. Hu, Z. Zhang, Humification improvement by optimizing particle size of bulking agent and relevant mechanisms during swine manure composting, Bioresour. Technol. 367 (2023) 128191, https://doi.org/10.1016/j.biortech.2022.128191.
[28] X. Gao, F. Yang, J. Cheng, Z. Xu, B. Zang, G. Li, X. Xie, W. Luo, Emission of volatile sulphur compounds during swine manure composting: source identification, odour mitigation and assessment, Waste Manag. 153 (2022) 129–137, https://doi.org/10.1016/j.wasman.2022.08.029.
[29] V.S. Varma, R. Parajuli, E. Scott, T. Canter, T.T. Lim, J. Popp, G. Thoma, Dairy and swine manure management – challenges and perspectives for sustainable treatment technology, Sci. Total Environ. 778 (2021) 146319, https://doi.org/10.1016/j.scitotenv.2021.146319.
[30] Q. Lang, B. Zhang, Z. Liu, Z. Chen, Y. Xia, D. Li, J. Ma, C. Gai, Co-hydrothermal carbonization of corn stalk and swine manure: combustion behavior of hydrochar by thermogravimetric analysis, Bioresour. Technol. 271 (2019) 75–83, https://doi.org/10.1016/j.biortech.2018.09.100.
[31] Q. Li, S. Zhang, M. Gholizadeh, X. Hu, X. Yuan, B. Sarkar, M. Vithanage, O. Mašek, Y.S. Ok, Co-hydrothermal carbonization of swine and chicken manure: influence of cross-interaction on hydrochar and liquid characteristics, Sci. Total Environ. 786 (2021), https://doi.org/10.1016/j.scitotenv.2021.147381.
[32] R.P. Ipiales, A.F. Mohedano, E. Diaz-Portuondo, E. Diaz, M.A. de la Rubia, Co-hydrothermal carbonization of swine manure and lignocellulosic waste: a new strategy for the integral valorization of biomass wastes, Waste Manag. 169 (2023) 267–275, https://doi.org/10.1016/j.wasman.2023.07.018.
[33] Q. Lang, Y. Guo, Q. Zheng, Z. Liu, C. Gai, Co-hydrothermal carbonization of lignocellulosic biomass and swine manure: hydrochar properties and heavy metal transformation behavior, Bioresour. Technol. 266 (2018) 242–248, https://doi.org/10.1016/j.biortech.2018.06.084.
[34] R. Ferrentino, G. Sacchi, D. Scrinzi, G. Andreottola, L. Fiori, Valorization of swine manure for a circular approach through hydrothermal carbonization, Biomass Bioenergy 168 (2023) 106689, https://doi.org/10.1016/j.biombioe.2022.106689.
[35] Q. Lang, M. Chen, Y. Guo, Z. Liu, C. Gai, Effect of hydrothermal carbonization on heavy metals in swine manure: speciation, bioavailability and environmental risk, J. Environ. Manag. 234 (2019) 97–103, https://doi.org/10.1016/j.jenvman.2018.12.073.
[36] J. bo Xiong, Z. qian Pan, X. feng Xiao, H. jun Huang, F. ying Lai, J. xin Wang, S. wei Chen, Study on the hydrothermal carbonization of swine manure: the effect of process parameters on the yield/properties of hydrochar and process water, J. Anal. Appl. Pyrolysis 144 (2019) 104692, https://doi.org/10.1016/j.jaap.2019.104692.
[37] C.S. Li, R.R. Cai, A. Hasan, X.L. Lu, X.X. Yang, Y.G. Zhang, Fertility assessment and nutrient conversion of hydrochars derived from co-hydrothermal carbonization between livestock manure and corn cob, J. Environ. Chem. Eng. 11 (2023) 109166, https://doi.org/10.1016/j.jece.2022.109166.
[38] M. Owsianiak, J. Brooks, M. Renz, A. Laurent, Evaluating climate change mitigation potential of hydrochars: compounding insights from three different indicators, GCB Bioenergy 10 (2018) 230–245, https://doi.org/10.1111/gcbb.12484.
[39] G. Ciceri, M. Hernandez Latorre, M. Kumar Mediboyina, F. Murphy, Hydorthermal Carbonization (HTC): Valorisation of Organic Waste and Sludges for Hydrochar Production and Biofertilizers, 2021.
[40] N. Davison, A. Brown, A. Ross, Potential greenhouse gas mitigation from utilising pig manure and grass for hydrothermal carbonisation and anaerobic digestion in the UK, EU, and China, Agriculture 13 (2023) 479, https://doi.org/10.3390/agriculture13020479.
[41] T.-S. Shin, S.-Y. Yoo, I.-K. Kang, N. Kim, S. Kim, H.-B. Lim, K. Choe, J.-C. Lee, H.-I. Yang, Analysis of hydrothermal solid fuel characteristics using waste wood and verification of scalability through a pilot plant, Processes 10 (2022) 2315, https://doi.org/10.3390/pr10112315.
[42] S.K. Hoekman, A. Broch, C. Robbins, R. Purcell, B. Zielinska, L. Felix, J. Irvin, Process development unit (PDU) for hydrothermal carbonization (HTC) of lignocellulosic biomass, Waste Biomass Valorization 5 (2014) 669–678, https://doi.org/10.1007/s12649-013-9277-0.
[43] T. Teribele, M. Costa, C. Sales da Silva, L. Pereira, L. Bernar, D. de Castro, F. da Costa Assunção, M. Santos, I. de Sousa Brandão, C. Fonseca, M. Shultze, T. Hofmann, S. Bremer, N. Machado, Hydrothermal carbonization of corn stover: structural evolution of hydro-char and degradation kinetics, Energies 16 (2023) 3217, https://doi.org/10.3390/en16073217.
[44] A.F. Mackintosh, H. Jung, I.-K. Kang, S. Yoo, S. Kim, K. Choe, Experimental study on hydrothermal polymerization catalytic process effect of various biomass through a pilot plant, Processes 9 (2021) 758, https://doi.org/10.3390/pr9050758.
[45] A. Mehli, D. Winkler, T. Griffin, S. Kaiser, A. Garcia, G. Gerner, B. Kulli, U. Baier, M. Kühni, A. Treichler, HTC Innovationscampus Rheinmühle - Pilotanlage zur Hydrothermalen Karbonisierung. https://doi.org/10.21256/zhaw-21929, 2021.
[46] M. Lucian, F. Merzari, A. Messineo, M. Volpe, Hydrothermal carbonization of sludge residues via carborem C700 industrial scale continuous operating plant, Chem. Eng. Trans. 92 (2022) 19–24, https://doi.org/10.3303/CET2292004.
[47] Technology — C-Green | OxyPower HTC™, (n.d.). https://www.c-green.se/oxypower-htc (accessed June 14, 2024).
[48] HTCycle, hydrothermal carbonis. A clean-running world, in: https://htcycle.ag/en/process_40, 2024. (Accessed 15 June 2024).
[49] TerraNova Energy Technology, Technol. HTC. (n.d.). https://www.terranova-energy.com/en/technology/(accessed June 15, 2024).
[50] M. Hitzl, Process of hydrothermal carbonization of biomass and installation for carrying out said process, 09825797.5/2 366 757. http://info.sipcc.net/files/patent/fulltext/EP/200605/EP2099194A1/EP2099194A1.PDF, 2012.
[51] Ingelia S.L., La planta HTC patentada por Ingelia, (n.d.). https://ingelia.com/index.php/planta-htc/carbonizacion-de-biomasa/(accessed June 14, 2024).
[52] J.J. Manyà, D. Alvira, M. Videgain, G. Duman, J. Yanik, Assessing the importance of pyrolysis process conditions and feedstock type on the combustion performance of agricultural-residue-derived chars, Energy Fuels 35 (2021) 3174–3185, https://doi.org/10.1021/acs.energyfuels.0c04180.
[53] A. Sadezky, H. Muckenhuber, H. Grothe, R. Niessner, U. Pöschl, Raman microspectroscopy of soot and related carbonaceous materials: spectral analysis and structural information, Carbon N. Y. 43 (2005) 1731–1742, https://doi.org/10.1016/j.carbon.2005.02.018.
[54] D. Antorán, D. Alvira, M.E. Peker, H. Malón, S. Irusta, V. Sebastián, J.J. Manyà, Waste hemp hurd as a sustainable precursor for affordable and high-rate hard carbon-based anodes in sodium-ion batteries, Energy Fuel. 37 (2023) 9650–9661, https://doi.org/10.1021/acs.energyfuels.3c01040.
[55] N. Pianta, D. Locatelli, R. Ruffo, Cycling properties of Na3V2(PO4)2F3 as positive material for sodium-ion batteries, Ionics 27 (2021) 1853–1860, https://doi.org/10.1007/s11581-021-04015-y.
[56] D. Alvira, D. Antorán, M. Vidal, V. Sebastian, J.J. Manyà, Vine shoots-derived hard carbons as anodes for sodium-ion batteries: role of annealing temperature in

regulating their structure and morphology, Batter. Supercaps. (2023), https://doi.org/10.1002/batt.202300233.
[57] M. Heidari, A. Dutta, B. Acharya, S. Mahmud, A review of the current knowledge and challenges of hydrothermal carbonization for biomass conversion, J. Energy Inst. 92 (2019) 1779–1799, https://doi.org/10.1016/j.joei.2018.12.003.
[58] D. Kim, K. Lee, K.Y. Park, Upgrading the characteristics of biochar from cellulose, lignin, and xylan for solid biofuel production from biomass by hydrothermal carbonization, J. Ind. Eng. Chem. 42 (2016) 95–100, https://doi.org/10.1016/j.jiec.2016.07.037.
[59] M. Tsarpali, J.N. Kuhn, G.P. Philippidis, Hydrothermal carbonization of residual algal biomass for production of hydrochar as a biobased metal adsorbent, Sustainability 14 (2022) 455, https://doi.org/10.3390/su14010455.
[60] Q. Gao, M.-M. Titirici, Achieving high volumetric EDLC carbons via hydrothermal carbonization and cyclic activation, JPhys Energy 2 (2020) 025005, https://doi.org/10.1088/2515-7655/ab60e6.
[61] N. Sun, Z. Guan, Y. Liu, Y. Cao, Q. Zhu, H. Liu, Z. Wang, P. Zhang, B. Xu, Extended "adsorption–insertion" model: a new insight into the sodium storage mechanism of hard carbons, Adv. Energy Mater. 9 (2019) 1901351, https://doi.org/10.1002/aenm.201901351.
[62] N. Nieto, J. Porte, D. Saurel, L. Djuandhi, N. Sharma, A. Lopez-Urionabarrenechea, V. Palomares, T. Rojo, Use of hydrothermal carbonization to improve the performance of biowaste-derived hard carbons in sodium ion-batteries, ChemSusChem (2023), https://doi.org/10.1002/cssc.202301053.
[63] S. Xie, T. Zhang, A. Mishra, A. Tiwari, N.S. Bolan, Assessment of catalytic thermal hydrolysis of swine manure slurry as liquid fertilizer: insights into nutrients and metals, Front. Environ. Sci. 10 (2022) 1–12, https://doi.org/10.3389/fenvs.2022.1005290.
[64] Y. Li, M. Chen, B. Liu, Y. Zhang, X. Liang, X. Xia, Heteroatom doping: an effective way to boost sodium ion storage, Adv. Energy Mater. 10 (2020) 2000927, https://doi.org/10.1002/aenm.202000927.
[65] C. Bommier, T.W. Surta, M. Dolgos, X. Ji, New mechanistic insights on Na-ion storage in nongraphitizable carbon, Nano Lett. 15 (2015) 5888–5892, https://doi.org/10.1021/acs.nanolett.5b01969.
[66] Y. Zheng, Y. Lu, X. Qi, Y. Wang, L. Mu, Y. Li, Q. Ma, J. Li, Y.S. Hu, Superior electrochemical performance of sodium-ion full-cell using poplar wood derived hard carbon anode, Energy Storage Mater. 18 (2019) 269–279, https://doi.org/10.1016/j.ensm.2018.09.002.
[67] X. Yin, Z. Lu, J. Wang, X. Feng, S. Roy, X. Liu, Y. Yang, Y. Zhao, J. Zhang, Enabling fast Na+ transfer kinetics in the whole-voltage-region of hard-carbon anodes for ultrahigh-rate sodium storage, Adv. Mater. 34 (2022) 2109282, https://doi.org/10.1002/adma.202109282.
[68] D. Ledwoch, L. Komsiyska, E.M. Hammer, K. Smith, P.R. Shearing, D.J.L. Brett, E. Kendrick, Determining the electrochemical transport parameters of sodium-ions in hard carbon composite electrodes, Electrochim. Acta 401 (2022) 139481, https://doi.org/10.1016/J.ELECTACTA.2021.139481.
[69] A. Agrawal, S. Janakiraman, K. Biswas, A. Venimadhav, S.K. Srivastava, S. Ghosh, Understanding the improved electrochemical performance of nitrogen-doped hard carbons as an anode for sodium ion battery, Electrochim. Acta 317 (2019) 164–172, https://doi.org/10.1016/j.electacta.2019.05.158.
[70] C. Ke, R. Shao, Y. Zhang, Z. Sun, S. Qi, H. Zhang, M. Li, Z. Chen, Y. Wang, B. Sa, H. Lin, H. Liu, M. Wang, S. Chen, Q. Zhang, Synergistic engineering of heterointerface and architecture in new-type ZnS/Sn heterostructures in situ encapsulated in nitrogen-doped carbon toward high-efficient lithium-ion storage, Adv. Funct. Mater. 32 (2022), https://doi.org/10.1002/adfm.202205635.
[71] J. Chong, S. Xun, H. Zheng, X. Song, G. Liu, P. Ridgway, J.Q. Wang, V.S. Battaglia, A comparative study of polyacrylic acid and poly(vinylidene difluoride) binders for spherical natural graphite/LiFePO4 electrodes and cells, J. Power Sources 196 (2011) 7707–7714, https://doi.org/10.1016/j.jpowsour.2011.04.043.
[72] S. Müllner, T. Michlik, M. Reichel, T. Held, R. Moos, C. Roth, Effect of water-soluble CMC/SBR binder ratios on Si-rGO composites using μm- and nm-sized silicon as anode materials for lithium-ion batteries, Batteries 9 (2023) 248, https://doi.org/10.3390/batteries9050248.
[73] Y. Li, F. Wu, Y. Li, M. Liu, X. Feng, Y. Bai, C. Wu, Ether-based electrolytes for sodium ion batteries, Chem. Soc. Rev. 51 (2022) 4484–4536, https://doi.org/10.1039/d1cs00948f.
[74] M. Goktas, C. Bolli, J. Buchheim, E.J. Berg, P. Novák, F. Bonilla, T. Rojo, S. Komaba, K. Kubota, P. Adelhelm, Stable and unstable diglyme-based electrolytes for batteries with sodium or graphite as electrode, ACS Appl. Mater. Interfaces 11 (2019) 32844–32855, https://doi.org/10.1021/acsami.9b06760.
[75] J. Fondard, E. Irisarri, C. Courrèges, M.R. Palacin, A. Ponrouch, R. Dedryvère, SEI composition on hard carbon in Na-ion batteries after long cycling: influence of salts (NaPF 6 , NaTFSI) and additives (FEC, DMCF), J. Electrochem. Soc. 167 (2020) 070526, https://doi.org/10.1149/1945-7111/ab75fd.
[76] M. Ma, H. Cai, C. Xu, R. Huang, S. Wang, H. Pan, Y.S. Hu, Engineering solid electrolyte interface at nano-scale for high-performance hard carbon in sodium-ion batteries, Adv. Funct. Mater. 31 (2021) 1–9, https://doi.org/10.1002/adfm.202100278.
[77] H. Kumar, E. Detsi, D.P. Abraham, V.B. Shenoy, Fundamental Mechanisms of Solvent Decomposition Involved in Solid-Electrolyte Interphase Formation in Sodium Ion Batteries, Chem. Mater. 28 (2016) 8930–8941, https://doi.org/10.1021/acs.chemmater.6b03403.
[78] K. Li, J. Zhang, D. Lin, D.W. Wang, B. Li, W. Lv, S. Sun, Y.B. He, F. Kang, Q.H. Yang, L. Zhou, T.Y. Zhang, Evolution of the electrochemical interface in sodium ion batteries with ether electrolytes, Nat. Commun. 10 (2019) 1–10, https://doi.org/10.1038/s41467-019-08506-5.
[79] Z.W. Seh, J. Sun, Y. Sun, Y. Cui, A highly reversible room-temperature sodium metal anode, ACS Cent. Sci. 1 (2015) 449–455, https://doi.org/10.1021/acscentsci.5b00328.
[80] X. Yin, Z. Wang, Y. Liu, Z. Lu, H. Long, T. Liu, J. Zhang, Y. Zhao, Insight into the influence of ether and ester electrolytes on the sodium-ion transportation kinetics for hard carbon, Nano Res. 16 (2023) 10922–10930, https://doi.org/10.1007/s12274-023-5793-9.
[81] S. Wu, H. Peng, J. Xu, L. Huang, Y. Liu, X. Xu, Y. Wu, Z. Sun, Nitrogen/phosphorus co-doped ultramicropores hard carbon spheres for rapid sodium storage, Carbon N. Y. 218 (2024) 118756, https://doi.org/10.1016/j.carbon.2023.118756.
[82] R. Xu, N. Sun, H. Zhou, X. Chang, R.A. Soomro, B. Xu, Hard carbon anodes derived from phenolic resin/sucrose cross-linking network for high-performance sodium-ion batteries, Batter. Energy. 2 (2023) 20220054, https://doi.org/10.1002/bte2.20220054.
[83] H. Darjazi, L. Bottoni, H.R. Moazami, S.J. Rezvani, L. Balducci, L. Sbrascini, A. Staffolani, A. Tombesi, F. Nobili, From waste to resources: transforming olive leaves to hard carbon as sustainable and versatile electrode material for Li/Na-ion batteries and supercapacitors, Mater. Today Sustain. 21 (2023) 100313, https://doi.org/10.1016/j.mtsust.2022.100313.
[84] H. Darjazi, A. Staffolani, L. Sbrascini, L. Bottoni, R. Tossici, F. Nobili, Sustainable anodes for lithium- and sodium-ion batteries based on coffee ground-derived hard carbon and green binders, Energies 13 (2020) 6216, https://doi.org/10.3390/en13236216.
[85] F. Zeng, L. Xing, W. Zhang, Z. Xie, M. Liu, X. Lin, G. Tang, C. Mo, W. Li, Innovative discontinuous-SEI constructed in ether-based electrolyte to maximize the capacity of hard carbon anode, J. Energy Chem. 79 (2023) 459–467, https://doi.org/10.1016/j.jechem.2022.12.044.
[86] H. Kim, J. Hong, Y.U. Park, J. Kim, I. Hwang, K. Kang, Sodium storage behavior in natural graphite using ether-based electrolyte systems, Adv. Funct. Mater. 25 (2015) 534–541, https://doi.org/10.1002/adfm.201402984.